Prediction of Seeded Free-Electron Laser Spectral Properties with a Time-dependent Theoretical Model

A thesis presented for the degree of Bachelor of Science

Lena Emily Linsner

Department of Physics

Division of Synchrotron Radiation Research

Supervisors:

Francesca Curbis,
Lund University, Division of Synchrotron Radiation Research
Enrico Allaria,
Elettra Sincrotrone Trieste

Project duration: 2 months
Examination date: May 2026

Acknowledgments

First and foremost, I would like to express my sincere gratitude to my supervisors, Francesca Curbis and Enrico Allaria, for offering me the opportunity to work on this project and for all the time and effort they invested in guiding me throughout it. I truly enjoyed working with you, and both the project itself and the challenges that came with it were immensely rewarding. I appreciate your patience in answering my many questions - even when I asked about the same concept multiple times - as well as your detailed and prompt replies to all my e-mails and the many extensive discussions that helped me develop a deeper understanding of the subject and encouraged me to bring forward my own ideas.

Moreover, I would like to thank my parents, who have always been my greatest supporters and who raised me to stay curious and determined. Thank you for never questioning my not-so-straight path, no matter how often I announced that it was again time for me to study something new. Finally, I would like to thank my partner for believing in me when I struggle to do so myself, and especially for the patience shown while listening to me talk for hours about tiny (and probably not very interesting) details of all my projects.

Abstract

A Free-Electron Laser (FEL) is a light source capable of producing extremely brilliant light pulses over a wide spectral bandwidth, with pulse lengths ranging from a few hundred picoseconds down to the femtosecond time scale. These pulses are generated and amplified through the interaction of a relativistic electron beam with a co-propagating radiation field in an undulator, a process either starting from shot noise or from an external seed laser.

While the full FEL process requires complex simulations to be described, a theoretical model has been proposed that allows to predict the output of an externally seeded FEL based on the electron beam and seed laser parameters to a high accuracy. This model has been proven to be a useful diagnostic tool to retrieve electron beam and seed laser parameters that are otherwise hard to access. However, the model's predictive accuracy fluctuates throughout the input parameter space. It was the main goal of this Bachelor project to classify regions within a limited parameter subspace to yield "valid" or "invalid" predictions based on the accuracy of these predictions, and to further investigate probable reasons for the failure of the model for parameters that are significantly far from the nominal values.

The study was based on systematic comparison of the model's predictions to simulations, accompanied by validation against experimental data. For the parameter configurations studied, the results indicated that in cases where the seed laser power strongly exceeds the nominal value, there is a large discrepancy ($\Delta > 20\%$) between the parameter values predicted by the model and those used in simulations. This is most likely due to saturation effects not yet included in the model and changes in the accumulated dispersion along the undulators that is assumed to be constant in the model.

Conversely, regions in which the model's predictions are of high to intermediate accuracy (deviations $\Delta \leq 10\%$ and $10\% < \Delta \leq 20\%$, respectively) were successfully determined. This was the case for constellations with low to intermediate values of both the energy spread of the electron beam ($\sigma_E \approx 30 - 60$ keV) and the seed laser power ($P < 200$ MW).

As expected, it was demonstrated that the model fails for parameter constellations yielding an initial bunching too low to overcome a startup from shot noise, a mechanism not included in the model. The studies show that in these cases, the pulse energy of the FEL is very low, allowing to identify unfavorable parameter sets a priori.

List of Acronyms

FEL Free-Electron Laser.

FERMI Free Electron Laser Radiation for Multidisciplinary Investigations.

HGHG High-Gain Harmonic Generation.

Linac Linear Accelerator.

SASE Self-Amplified Spontaneous Emission.

XFEL X-ray Free-Electron Laser.

Contents

1 Introduction

The FEL principle was introduced by J. Madey in 1971 [11]. His publication proposed the theoretical outline of how a beam of electrons passing through a periodic magnetic field could emit coherent radiation. Using "free" relativistic electrons as a gain medium instead of electrons bound to atoms or molecules was a genuinely novel idea at that time. Later in the 1970s, Madey and his coworkers built the first FEL at Stanford University, operating in the infrared at a wavelength of 12 μm [15]. However, for many years FELs played only a marginal role next to conventional quantum lasers. Only in the 1990s the understanding evolved that an FEL is an extremely powerful light source that can even be operated in the X-ray regime, contrary to quantum lasers. The first X-ray Free-Electron Laser (XFEL) operating in the soft X-Ray was built in the early 2000s in Hamburg, and started user operation under the name FLASH in 2005 [16]. Later in 2009 the first stable XFEL at hard X-Ray started operating in Stanford, known as the Linac Coherent Light Source (LCLS) [5].
As XFELs can reach a peak brilliance up to 8 orders of magnitude higher than any other X-ray source, and further are able to generate pulses on the femtosecond timescale, they have proven to be an invaluable instrument, for example to investigate the structure of individual bio-molecules [15]. Hence, they opened a field inaccessible to researches before, leading to more XFEL construction around the globe and further development of the principles [12].

The FEL requirements on the electron beam quality are demanding, such that currently only a Linear Accelerator (Linac) is able to provide the beam. This relativistic high quality beam of electrons is guided from the accelerator output to an undulator magnet, which is a series of alternating dipole magnets. These modify the longitudinal motion of the electrons to acquire a transverse component, allowing for a coupling of the electrons to a co-propagating radiation field [4]. Depending on the specific FEL setup, this radiation field can originate either from shot noise, in a process called Self-Amplified Spontaneous Emission (SASE) [3, 9], or from a seed laser, e.g. in High-Gain Harmonic Generation (HGHG) [22]. The latter is a seeding scheme based on a seed laser in combination with a short undulator and a magnetic chicane to initiate the FEL process.
Independent of the FEL startup mechanism, the resulting interaction between the electrons and the light field leads to strong amplification of the field, ultimately producing a powerful FEL pulse.

Recently, a theoretical model has been developed [13] that predicts the FEL spectrum and energy per pulse in HGHG, which is the seeding scheme used at the FEL facility called Free Electron Laser Radiation for Multidisciplinary Investigations (FERMI) in Trieste, Italy, operating in the ultraviolet and soft X-ray regime.
The capability of this model to reproduce the evolution of spectral and intensity features as well as the FEL energy per pulse upon varying the chicane strength as observed in experiments and simulations has been demonstrated [1, 13].
The HGHG FEL critically depends on a range of electron beam and seed laser parameters, which influence not only the FEL intensity but also the temporal and spectral properties of the generated radiation. Previous studies have demonstrated the model's ability to accurately reproduce these dependencies near nominal parameter values; however, a comprehensive assessment of its performance far from these conditions is still lacking, even though some parameter constellations are known to lead to large deviations of the predictions of the model compared to simulations, leading to unreliable results for given settings.
Therefore, this study investigates the model's behavior across a limited parameter subspace. To this end, we focus on the most influential parameters affecting FEL performance and validate the model predictions systematically against full numerical simulations over a wide parameter range, accompanied by a qualitative validation against experimental data collected at FERMI.

In particular, this study aims to define a validity range of the investigated parameters and to find the accuracy of the model's predictions in different regions of the chosen parameter space. Moreover, by exposing probable underlying reasons for the failure of the model in specific regions of the parameter space, this project is meant to serve as a foundation for future extensions of the model.

2 Theoretical Background

2.1 Free-Electron Lasers

2.1.1 General Working Priciple

Unlike a conventional laser, the working principle of an FEL is not based on stimulated emission from an atomic system with a population inversion, but rather on unbound - *free* - electrons that interact with a radiation field in an undulator magnet (cf. Section 2.1.3) [4]. Consequently, a relativistic electron beam acts as both the energy pump and the active lasing medium. The sinusoidal magnetic field of the undulator forces the electrons onto an oscillatory trajectory, introducing a transverse velocity component that enables sustained energy transfer from the electron beam to a co-propagating radiation field [15]. This radiation field may originate from either shot noise or an external seed laser. Under suitable beam conditions, the interaction gives rise to a collective instability, resulting in coherent amplification of the radiation field along the undulator and the generation of an intense FEL pulse. The overall gain and FEL output power depend on the undulator configuration and length as well as the properties of the electron beam and, in seeded FELs, the seed laser parameters.
Therefore, two key components of the FEL system to be discussed in the following are the electron beam, which must satisfy stringent requirements, and the undulator, which determines the interaction.

2.1.2 Electron Beam Requirements

The requirement for relativistic electron energies is closely related to the relativistic Doppler effect, which leads to a strong blue-shift of the emitted radiation wavelength as seen by an observer in the laboratory frame looking against the beam. Further, the relativistic nature confines the emission to a narrow forward cone [15], a feature common to synchrotron radiation. The FEL wavelength depends, among other factors, on the central or nominal energy of the electron beam E_0, where a higher E_0 yields a shorter wavelength. The nominal beam energy is typically on the order of a few GeV for an FEL operating in the soft X-ray, while for a hard X-ray FEL E_0 reaches 10 - 20 GeV.

Additionally, the FEL process relies on a collective instability that develops only when the electron beam has a sufficiently high peak current I and suitable beam quality, which is currently only achieved by a Linac [15]. Therefore, typical peak currents range from 500 A to 5 kA.
Further, the electron beam consists of bunches of finite length, the generation of which at the gun is a stochastic process. This, together with other non-linear effects developing in the low energy regime of the acceleration process, leads to the electron bunch acquiring a finite energy spread, commonly described by its rms value σ_E [10]. The respective Lorentz factor is defined as $\gamma = E_0/(m_e c^2)$, where m_e is the electron rest mass [15].
Another quality defining electron beam parameter is the emittance ϵ. In accelerator physics, the electron state is commonly described by a vector in a six-dimensional phase space consisting of real-space coordinates and, in approximation, the respective momenta, as explained in more detail in Section 2.1.6. The electrons in a beam occupy a certain region in this phase space. Projected onto three 2D subspaces, vertical (y, y'), horizontal (x, x'), and longitudinal (z, δ), these

particles are approximately confined within an ellipse in each of these subspaces [18]. These ellipses define three independent two-dimensional beam emittances proportional to the area A of the ellipse in the respective subspace as $\epsilon_i = A_i/\pi$, where i refers to the plane. The emittance is a means to describe how "spread out" the beam is in phase space: a small emittance means a higher brightness of the beam in real space, i.e. a high electron density in a small area with low momentum spread. To account for energy-dependent changes in longitudinal phase space as the electrons are accelerated, the normalized emittance in the respective subspace is introduced as $\epsilon_{n,i} = \gamma\beta\epsilon_i$, where $\beta = v/c$ is the relative particle velocity.
The transverse emittance is tightly linked to the rms transverse beam size in real space in the linear approximation as $\sigma_{x,y} = \sqrt{\beta_{x,y}\epsilon_{x,y}}$, where $\beta_{x,y}$ is a parameter related to the shape of the ellipse in phase space [18]. Typical values for the normalized emittance $\epsilon_{n,i}$ are around 1 mm·mrad.

The requirements of the FEL on the electron beam quality in terms of a small transverse beam size, high peak current and low energy spread are especially demanding. A small transverse beam size and a high peak current are crucial for a powerful FEL output, while a low energy spread is important for generating coherent radiation [15].

2.1.3 Electron - Radiation Interaction in an Undulator

In an FEL, the relativistic electron beam produced in the Linac acts as the energy pump. However, energy transfer between the electron beam and a co-propagating radiation field is not possible if the direction of propagation of the beam is orthogonal to the field. Hence, the electrons are sent on a curved trajectory in order for the particles to acquire a velocity component along the field direction, giving $dW/dt = \mathbf{v} \cdot \mathbf{F} \neq 0$ [15].
This is typically achieved by an undulator, which consists of a periodic sequence of short dipole magnets of alternating polarization. This setup gives rise to a sinusoidal magnetic field along the undulator axis, which in turn introduces sinusoidal transverse deflections of the electron beam path [19]. The trajectory of the electrons depends on the properties of the undulator, in particular the field strength of the dipole magnets B_0 and the period λ_u of the magnetic arrangement. In this context, a dimensionless undulator parameter K is introduced as [15]

$$K = \frac{eB_0}{m_e c k_u}, \tag{1}$$

where e is the elementary charge, m_e the rest mass of an electron, c the speed of light, and $k_u = 2\pi/\lambda_u$. Generally, $K \leq 1$ for undulator magnets [19].
A co-propagating radiation field will in general slip forward by a distance λ_r per undulator period with respect to the electrons in the beam due to their finite velocity, an effect known as slippage. This distance is given by the undulator's resonant wavelength

$$\lambda_r = \frac{\lambda_u}{2\gamma^2}\left(1 + \frac{K^2}{2}\right), \tag{2}$$

where γ is the Lorentz factor corresponding to the nominal beam energy [12]. As this slippage effect is periodic, co-propagating radiation with wavelength $\lambda_l \simeq \lambda_r$ will constructively interfere after many undulator periods, resulting in sustained energy transfer from the electron beam to the radiation field [8].

2.1.4 High-Gain FEL Theory

In the case of a very long undulator, the radiation field amplitude will grow considerably due to an extended interaction with the electron beam. The underlying mechanism is described in high-gain FEL theory.

The large power gain is closely related to the evolution of a microbunch structure in the electron beam, i.e. a periodic charge density modulation on the scale of the co-propagating radiation wavelength λ_l. The electrons accumulated within one microbunch will emit coherently, and since all microbunches are separated by λ_l, the radiation from successive microbunches adds constructively. As a result, the intensity of the radiation field is proportional to the number of particles squared, $I \propto N^2$, which is greater by a factor of N compared to incoherent radiation. The consequence is a stronger radiation field, which will further enhance the microbunching, yielding an exponentially growing radiation power [15].
Microbunching in an FEL can originate from two different sources: The first is by spontaneous incoherent emission of the electrons passing through the undulator, called SASE [2]. The second possible origin is by interaction of a seed laser of wavelength λ_l and the electron bunch in a short undulator [8], which is further discussed in Section 2.1.5.

In theory, the time evolution of a system consisting of the electrons in a bunch and a radiation field is described by four self-consistent coupled first-order differential equations. However, due to the large number of electrons per bunch, these result in a complicated many-body problem to which no analytical solution exists. If the periodic charge density modulation of the electron beam can be assumed small, a single third-order differential equation can be derived from the first-order equations by perturbation theory [15]. This equation contains only the amplitude of the electric field of the light wave and can be solved analytically. The solution reveals that the FEL interaction can be described by a single parameter, the so-called FEL or Pierce parameter ρ_{FEL}. This dimensionless parameter characterizes the strength of the coupling between the electron beam and the radiation field and combines the relevant beam and undulator parameters into a single quantity. At this point, it is helpful to introduce the gain length $L_{g0} = \lambda_u/(4\pi\sqrt{3}\rho_{\mathrm{FEL}})$ of an FEL. It describes the undulator length needed to achieve an increase in the FEL power by a factor of e [8]. Here, the subscript 0 indicates the validity of this definition only in idealized 1D-theory, while for a realistic gain length the relation $L_g > L_{g0}$ holds. From the third-order equation the power of the FEL at position z along the undulator is then found to be [15]

$$P_{\mathrm{FEL}}(z) \propto \exp\left(\frac{z}{L_{g0}}\right). \tag{3}$$

This proportionality yields three distinct phases of power growth along the undulator, which is consequently called a radiator. The first section of the radiator is characterized by lethargy, where the FEL power remains approximately constant or grows only weakly [3]. Typically, this holds for longitudinal coordinates $z \leq 3L_{g0}$. This regime is followed by exponential power growth, driven by the self-reinforcing feedback between the microbunching and the radiation field [15]. Eventually, the effect will saturate after about 20 gain lengths [7]. At this point, the electrons are strongly bunched and consequently start re-gaining energy from the radiation field [12].
The final resulting FEL saturation power can be related to ρ_{FEL} by

$$P_{\mathrm{sat}} \sim 1.6 \cdot \rho_{\mathrm{FEL}} \cdot P_{\mathrm{beam}}, \tag{4}$$

where P_{beam} is the peak power of the electron beam [7].

2.1.5 FEL Seeding via High-Gain Harmonic Generation

As mentioned above, one possibility of inducing microbunching to the electron beam is seeding by an external radiation source, typically with a high degree of longitudinal coherence [7]. To seed an FEL in the extreme ultraviolet or an XFEL an intense laser-like source is needed. However, there exist no conventional lasers with enough power at such short wavelengths, and hence alternative processes have been developed [15]. One such seeding approach for an XFEL is the so-called High-Gain Harmonic Generation (HGHG), which has been first suggested by L. Yu [22]. This seeding scheme is used at FERMI and Figure 1 illustrates its principle.

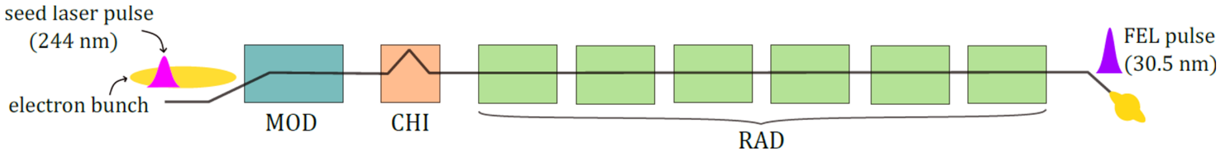

Figure 1: Schematic of the HGHG scheme used at FERMI. The electron bunch is sent through the modulator (MOD) together with the seed laser pulse, resulting in an energy modulation that is converted to a charge density modulation in the chicane (CHI). The radiator (RAD) is tuned to the desired harmonic that is then amplified.

An external seed laser with wavelength λ_s is injected and passes a short undulator, called modulator, together with the electron bunch. In the modulator, which is tuned to the seed wavelength λ_s, the seed laser pulse interacts with the electrons and introduces a periodic energy modulation to the bunch. This energy modulation is then converted to a corresponding periodic charge density modulation by a dispersive section placed after the modulator, typically a magnetic chicane [7, 8]. The result is a periodic charge density modulation with period λ_s. Moreover, this density modulation contains a significant content of higher harmonics h of the seed laser wavelength λ_s [7]. By tuning the radiator following the chicane to $\lambda_r = \lambda_s/h$, the FEL output is driven by the h-th harmonic component of the bunching [1]. Therefore, radiation at a much shorter wavelength than the seed laser can be amplified in the FEL process.
The ranges of the electron beam, seed laser, and undulator parameters at FERMI are summarized in Table 1, together with the values used in this project.

Table 1: Electron beam, seed laser and undulator/chicane parameters typically used at FERMI. Given are the standard value range together with the values used in this study.

Parameter	Symbol	Standard value range	Used values
Electron Beam Parameters			
Energy	E_0	0.9–1.55 GeV	1.35 GeV
Energy spread (rms)	σ_E	40–100 keV	60 keV
Peak current	I	500–700 A	700 A
Norm. emittance	ϵ_n	1.0–2.0 mm·mrad	1.5 mm·mrad
Average beamsize	σ_x	50–100 μm	80 μm
Seed Laser Parameters			
Wavelength	λ_s	240–265 nm	244 nm
Pulse duration	τ_0	70–150 fs	100 fs
Peak power	P	25–400 MW	100 MW
Waist	w_s	0.5–2.0 mm	1.05 mm
Harmonic	h	3–15	8
Undulator and Chicane Parameters			
Modulator undulator period	$\lambda_{u,\mathrm{mod}}$	0.1 m	0.1 m
Modulator undulator length	$L_{u,\mathrm{mod}}$	3.0 m	3.0 m
Radiator undulator period	$\lambda_{u,\mathrm{rad}}$	0.055 m	0.055 m
Radiator undulator length	$L_{u,\mathrm{rad}}$	2.42 m	2.42 m
Number of radiators	n_{rad}	1–6	3
Active radiator length	L_{rad}	2.42–15.52 m	7.26 m
Radiator polarization	–	linear, circular	circular
Chicane dispersion	R_{56}	0–250 μm	0–250 μm

2.1.6 Matrix Formalism of Charge Density Modulation by a Chicane

A chicane typically consists of an arrangement of four dipole magnets as illustrated by Figure 2 [8]. As a non mono-energetic electron bunch passes through the chicane, the path lengths of the individual particles are inversely proportional to their energy. Hence, a chicane effectively converts an energy modulation to a charge density modulation [7].

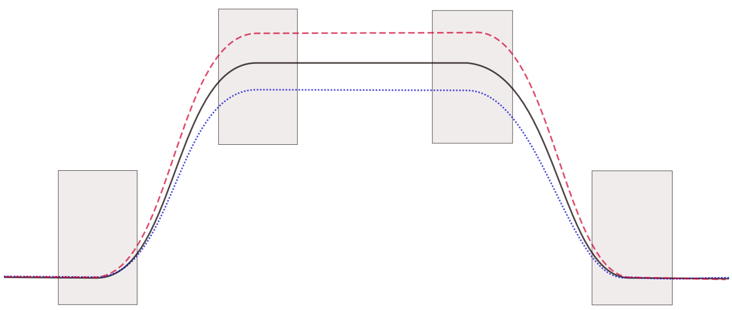

Figure 2: Schematic of a chicane and trajectories of nominal electrons (black solid line), electrons with slightly lower energy (red dashed line), and electrons with slightly higher energy (blue dotted line). The gray rectangles represent the dipole magnets.

The underlying dynamics are represented by a matrix formalism. The electron state is commonly described by a vector $\mathbf{X}$ in a six-dimensional phase space, where [10]

$$\mathbf{X} = \begin{pmatrix} x \\ x' \\ y \\ y' \\ z \\ \delta \end{pmatrix}. \tag{5}$$

Here, x, y are the transverse and z the longitudinal coordinates, respectively, while $x' = dx/dz \approx p_x/p_z$, $y' = dy/dz \approx p_y/p_z$ represent the corresponding normalized transverse momentum components. In approximation, x' and y' represent the angles of the particle trajectory with respect to the longitudinal axis. Further, $\delta = \Delta\gamma/\gamma$ denotes the energy deviation of a particle with respect to a nominal electron.
The evolution of the state vector $\mathbf{X}$ represents the dynamics of the electrons in phase space when passing an accelerator element such as a magnet. In linear approximation, the final electron state $\mathbf{X_f}$ is found by multiplication of a 6×6 transport matrix R with the initial state $\mathbf{X_i}$, i.e. [10]

$$\mathbf{X_f} = R \cdot \mathbf{X_i} = \begin{pmatrix} R_{11} & R_{12} & \cdots & R_{16} \\ R_{21} & R_{22} & \cdots & R_{26} \\ \vdots & \vdots & \ddots & \vdots \\ R_{51} & R_{52} & \cdots & R_{56} \\ R_{61} & R_{62} & \cdots & R_{66} \end{pmatrix} \cdot \begin{pmatrix} x_i \\ x'_i \\ y_i \\ y'_i \\ z_i \\ \delta_i \end{pmatrix}. \tag{6}$$

From this it is obvious that the correlation of the longitudinal coordinate z and the energy deviation δ is the given by the matrix element R_{56}, and in linear approximation $z_f = z_i + R_{56}\delta$ [18]. Hence, R_{56} serves as a measure of the dispersive strength of an accelerator element such as a chicane.
It has been shown that a scan of the dispersive strength R_{56} of the chicane placed after the modulator in a HGHG setup significantly influences both the temporal and spectral FEL outputs [6]. This is illustrated by Figure 3, which shows the FEL output for a range of R_{56} values as predicted by the simulation tool *Genesis-1.3* (cf. Section 3.3).

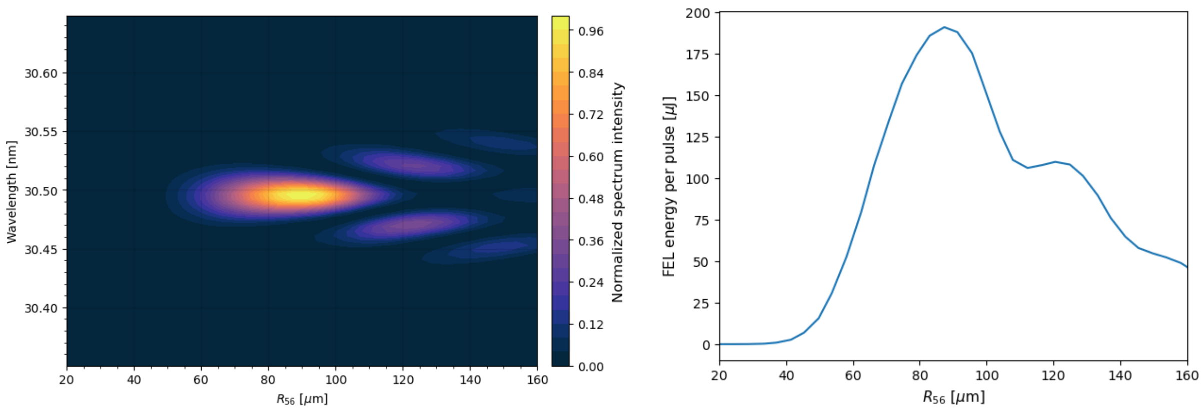

(a) (b)

Figure 3: Simulated FEL output for a scan of the dispersive strength of the chicane following the modulator in a HGHG setup. Shown are (a) the globally normalized spectrum intensity and (b) the energy per FEL pulse as functions of R_{56}. The electron beam, seed laser and undulator properties in this scan were set according to the values listed in the right column of Table 1.

Figure 3a shows the globally normalized FEL spectrum intensity per wavelength and R_{56} for a Fourier-limited seed laser pulse. The map displays the typical spectral splitting occurring at increased dispersive strength of the chicane, which is a result of overbunching. In this regime the longitudinal charge density distribution becomes strongly distorted, leading to substructures within one modulation period. This introduces additional Fourier components.
Figure 3b displays the energy per FEL pulse as a function of R_{56}. The pulse energy shows oscillating features that decrease in amplitude, which is typical for a time-dependent energy modulation [1].
In general, R_{56} is not exclusive to chicanes, as other accelerator elements such as undulators also introduce a longitudinal dispersion. However, this effect is usually small.

2.2 Theoretical Model for HGHG Spectral Analysis

A novel model has been proposed that efficiently determines the spectral properties and pulse energy of a HGHG seeded FEL with high accuracy [13]. It has been demonstrated that fitting the model output of the pulse energy as a function of chicane strength R_{56} to respective experimental measurements uniquely defines the electron beam energy spread σ_E, the beam peak current I and the seed laser energy E_s by extracting the first two peak energies and the chicane strength at which the first peak is observed [1]. This theoretical model is presented below according to [13].

It is common to define a dimensionless time-dependent energy modulation amplitude $A(t) = \Delta E(t)/\sigma_E$, where $\Delta E(t)$ is the energy modulation induced on the electron beam by the seed laser in the modulator of the HGHG section.
Analogously, the longitudinal dispersive strength of the chicane is quantified by a dimensionless bunching parameter $B = R_{56}k_s\sigma_E/E_0$. Here E_0 is the average energy of the electrons in the beam and $k_s = 2\pi/\lambda_s$ the wavenumber of the seed laser.
According to [6], the FEL output at harmonic h is driven by a dimensionless electron bunching factor

$$b_h(t) = e^{-h^2B^2/2}J_h[-hBA(t)]e^{ih[\phi_s(t)+\phi_e(t)]}, \tag{7}$$

where J_h is the Bessel function of the first kind of order h, and $\phi_s(t)$ and $\phi_e(t)$ account for the phases of the seed laser and the electrons, respectively. As the energy modulation amplitude $A(t)$ is proportional to the square root of the power of the seed laser, it can be expressed as

$$A(t) = A \cdot \sqrt{\exp\Big[-8\ln{(2)}t^2/(2\tau^2)\Big]}, \tag{8}$$

where A describes the peak value of the energy modulation, τ is the pulse duration of the seed laser at the full-width at half maximum (FWHM), under assumption of a Gaussian seed laser pulse.
The electron phase $\phi_e(t)$ includes a possible time-dependent energy profile of the electron beam $E(t)$, introduced by the Linac, as

$$\phi_e(t) = (B/\sigma_E)E(t). \tag{9}$$

The phase variation of the seed laser includes a possible linear frequency chirp if defined as

$$\phi_s(t) = (\alpha/2)t^2, \tag{10}$$

not considering higher order terms. Here, α is the chirp parameter, which is related to Group Delay Dispersion (GDD), which may be introduced to the seed laser pulse by an optical element, effectively stretching the original pulse length. Since the FEL power is proportional to the square of the bunching amplitude, $P \propto |b|^2$, the FEL spectrum is finally found by performing a

Fourier transform of $b_h(t)$ and subsequently computing $|b_h(k)|^2$.

It has been shown that the above described theoretical approach correctly reproduces the spectral splitting at increased dispersive strength R_{56} of the chicane as seen in experiments [6]. To predict changes in the FEL pulse energy for increasing R_{56} and to find absolute values for A and σ_E, the model has been extended to take the power growth occurring in the radiator into account, which is approximated by [7]

$$P(z) = P_{\mathrm{th}} \cdot \left[\frac{\frac{1}{3}(\frac{z}{L_g})^2}{1 + \frac{1}{3}(\frac{z}{L_g})^2} + \frac{\frac{1}{2}\exp\left(\frac{z}{L_g} - \sqrt{3}\right)}{1 + \frac{P_{\mathrm{th}}}{2P^*_{\mathrm{sat}}}\exp\left(\frac{z}{L_g} - \sqrt{3}\right)} \right]. \tag{11}$$

Here, z is the length of the radiator, L_g is the gain length, and $P^*_{\mathrm{sat}} = P_{\mathrm{sat}} - P_{\mathrm{th}}$ rescales the FEL saturation power P_{sat}. In turn, $P_{\mathrm{th}} = \rho_{\mathrm{FEL}} \cdot |b|^2 \cdot P_{\mathrm{beam}}$, which introduces the FEL parameter ρ_{FEL}, the initial bunching b, and the electron beam power P_{beam} to Eq. (11). Time-dependence enters through $b = b(t)$ as given by Eq. (7), and through considering a 3D approximation of L_g and P_{sat}, which both depend on the variation of the electron beam energy spread $\sigma_A(t) = \sigma_E\sqrt{1 + A(t)^2/2}$ as given by [20, 21]. Eq. (11) takes into account all three phases of the power growth - lethargy, exponential growth, and saturation.

As has been demonstrated, the above extension of the theoretical model leads to improved agreement with the experimental data [13] and can be used to obtain more realistic estimates for σ_E upon a fit of the model to the measurements [1].

3 Methodology

3.1 General Research Design and Parameter Space

This project investigated how the theoretical model presented in Section 2.2 behaves across selected beam and seed laser parameters through systematic simulations. In particular, the study targeted the identification of the model's validity range for these key parameters to provide a foundation for future model extensions and give an accuracy estimate for the predictions of the model in the determined valid parameter space regions. This was motivated by a small discrepancy that has been identified between the model output and the respective simulation prediction for the FEL energy per pulse, as well as by known limitations of the model. Figure 4 illustrates this discrepancy by showing both the model (orange) and simulation (blue) output for the FEL energy per pulse, where both cases were using the nominal FERMI electron beam and seed laser parameters.
The mentioned limitations include, among others, the incapability of the model to predict post saturation dynamics, as well as the fact that the resonance condition is not considered when calculating the laser induced modulation and the FEL amplification.
After the model validation based on the numerical simulations, experimental R_{56} scans aimed for validating the model output qualitatively under real operating conditions.

An implementation of the model was developed in Python to enable direct comparison of its predictions to both simulation and experiments. Since real FEL systems lack the accurate parameter control available in simulations, experimental measurements served as a qualitative comparison. In an FEL experiment, the underlying electron beam and seed laser parameters are measured and exhibit a high level of uncertainty. Hence, the final comparison of the model with experimental data was used to assess the robustness of the proposed procedure and fitting algorithm used in the simulations, as this real data is subject to instrumental noise and nonlinearities.

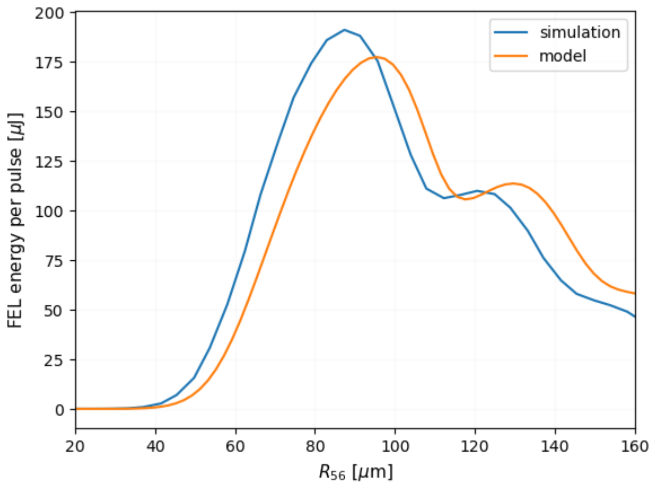

Figure 4: FEL energy per pulse as predicted by the model (orange) and a simulation (blue) for equal input parameters according to the rightmost column in Table 1.

In summary, the methodology consisted of three main parts: model implementation, simulation-based evaluation, and analysis of the experimental data. These steps are described in more detail in the following sections.

The investigated parameter space was limited to the rms energy spread of the electron beam σ_E, the electron beam peak current I, and the seed laser power P. These parameters are of particular interest because they significantly influence FEL behavior but cannot be precisely measured in experiments, assigning them a critical role in understanding the model predictions.

3.2 Python Implementation of the Theoretical Model

A Python implementation of the theoretical HGHG model described in Section 2.2 served as the basis for the subsequent analysis. For reproducibility, a structural diagram of the code is shown in Section A of the Appendix, together with further details on all parameters, helper functions and used classes.

The input parameters, according the the first column in Table 1, characterize the electron beam, the seed laser, and the FEL setup under consideration.
Upon execution of the code, the corresponding objects are initialized on the basis of the above inputs and then passed into a module performing the computations according to the model. In particular, the code evaluates the theoretical relations for a given dispersive strength of the chicane R_{56}, and computes the resulting FEL output. This output consists of the FEL spectrum in both time domain and frequency domain, and the pulse energy of the FEL, which are both properties that can be measured directly in an experiment. The spectral intensities are visualized as two-dimensional heatmaps, showing λ_{FEL} and time t versus R_{56}, respectively, while the FEL pulse energy is plotted as a function of R_{56} (cf. Figure 3), including normalization options for all plots to facilitate comparison. To investigate the dependence of the FEL output on the chicane strength, the code is vectorized and performs a scan over a specified range of R_{56} values simultaneously. Compared to simulation and experiment, the model implementation is much more time-efficient. Using it for reproducing an R_{56} scan takes a few seconds, while an experimental measurement takes about 5 minutes and the simulations may even proceed for a few hours.
Compared to the analytical formulation of the theoretical model, the code introduces additional

approximations. Firstly, a discrete grid is used for time t, where the model assumes a continuous variable, resulting in finite resolution of the computed observables. This grid may be optimized to minimize the computational time, which is on the order of seconds, while generating reliable results with high enough resolution. Further, the frequency domain spectrum of the FEL is obtained via fast Fourier transform (FFT) of the time domain signal, introducing a dependence of the result on the chosen temporal grid and the related finite signal window. Lastly, numerical integration over the finite pulse length is used to compute the pulse energy.

Moreover, it is important to note that the model approximates the FEL process in distinct steps: first the energy modulation, followed by the phase space rotation, and finally emission. In reality these processes are not fully separated, and electrons start to rotate in phase space and to produce bunching already in the modulator, and also in the radiator after passing the chicane. This introduces additional dispersion, which the model implementation accounts for by introducing an offset to the R_{56} of the chicane as 40% of the dispersion introduced by the modulator $R_{56,\mathrm{mod.}}$, following earlier studies of the model.
Furthermore, an additional offset of 0.5 μm was considered when evaluating the experimental data accounting for the residual non-zero field of the chicane magnets.

3.3 Simulations

For numerical reproduction of the R_{56} scans, the FEL simulation code *Genesis-1.3* was used [14]. *Genesis-1.3* is a fully three-dimensional, time-dependent code widely used in FEL studies. The simulations are based on a numerical solution of the coupled FEL equations describing the interaction between the electron bunch and the radiation field in an undulator. The standard approach of the program is a division of the electron bunch into longitudinal slices and tracking the evolution of the radiation field as well as the electron dynamics in each slice. *Genesis-1.3* enables accurate modeling of power gain and saturation effects occurring in the radiator, both for SASE and HGHG.

A factorial design of experiment was chosen for the defined parameter space to be able to both determine the effect of each parameter individually and assess possible parameter interactions. To this end, five values spanning the normal operating range were selected for σ_E, I and P, respectively, yielding a total of 125 simulations considering all possible combinations. An overview of these parameter values is given by Table 2.

Table 2: Values of σ_E, I and P used in the comparison of the model output to simulations. According to a factorial design of experiment, all 125 possible combinations of these values were used as inputs for the simulations.

σ_E (keV)	I (A)	P (MW)
30	300	25
45	500	50
60	700	100
90	900	200
150	1200	400

The remaining electron beam, seed laser and HGHG setup parameters were kept constant throughout the scans and set to the typical operating values listed in the rightmost column of Table 1. These values were chosen to be both within the valid operating range of the model and within the normal operating range of the system. To ensure a reliable comparison of the model outputs with the simulations, both the model implementation and *Genesis-1.3* used the same input parameters for each scan. Only Fourier-limited seed laser pulses were simulated.

Example input files as used in the *Genesis-1.3* simulations are presented in Section B of the appendix.

To quantify the accuracy of the model with respect to the simulation, the respective outputs for the FEL pulse energy were compared. To this end, the model's predictions were fitted as a function of σ_E, I and P to the *Genesis-1.3* output using `scipy.optimize.least_squares`, with simulation input values according to Table 2 as respective initial guess. Following earlier studies of the HGHG model, the range of the R_{56} grid used in the fit was limited to the first two peaks of the FEL pulse energy found from the simulation. This upper limit was set by multiplying the R_{56} corresponding to the first maximum by a factor of 1.7, which appeared to be a good approximation in most cases.

With the goal of defining regions of validity in the parameter subspace under investigation, the deviations between the parameter values predicted by the model upon fit from the simulation input parameters were then analyzed in detail. In this study "deviation" was defined as $\Delta p = p_{\text{fit}} - p_{\text{sim}}$, where $p \in \{\sigma_E, I, P\}$.

For each parameter deviation Δp, the analysis was conducted in the following three main steps. First, a one-dimensional baseline analysis was carried out to quantify the dependence of each deviation Δp on the three parameters p individually. To this end, one p at a time was varied across its full range as indicated by Table 2, while the remaining two parameters were held fixed at their nominal values, respectively ($\sigma_E = 60$ keV, $I = 700$ A, $P = 100$ MW). To provide an example, $\Delta\sigma_E$, ΔI and ΔP were found as functions of σ_E, while $I = 700$ A and $P = 100$ MW were kept at nominal.
Second, two-dimensional parameter interactions were investigated over the full parameter space. For each value pair of two parameters the mean deviation of the third parameter was computed. For example, $\langle\Delta\sigma_E\rangle$ was found at each point (I_j, P_k), where j, k refer to the respective values of I and P as indicated in Table 2 .
Third, to further resolve parameter coupling effects, the sensitivity of each Δp to p was investigated upon variation of the remaining two parameters, respectively. For example, $\Delta\sigma_E$ was found as a function of σ_E for each value I_j, yielding five lines (one per I_j). The value of $\Delta\sigma_E$ at each I_j was then averaged across all P_k.

To eventually separate the parameter space into valid and invalid regions, a sensible definition of validity was required. A first discrimination was introduced based on the FEL pulse energy. Configurations resulting in a pulse energy lower than 15 μJ were defined as invalid, as they do not guarantee the model's ability to properly reproduce the data. Therefore, these were excluded from the analysis.
Further, the parameter values predicted by the model should yield a high accuracy. Hence, the following classification was applied as a secondary discrimination: points in parameter space with an absolute deviation $\Delta\sigma_E \leq 10$ keV and relative deviations $\Delta I \leq 10\%$, $\Delta P \leq 10\%$ are labeled as highly accurate. Points with $10 < \Delta\sigma_E \leq 20$ keV, $10\% < \Delta I \leq 20\%$ and $10\% < \Delta P \leq 20\%$ are classified as valid points with low accuracy. The remaining points are classified as invalid, together with all points resulting in a too weak FEL output.

3.4 Experimental Data

A series of R_{56} scans with different settings on the electron beam and seed laser parameters was conducted at FEL-1 at FERMI. Such a scan is a standard procedure and can be easily performed using the respective panels in the control room and detecting the resulting FEL spectrum and energy per pulse. The former is measured by using a grating spectrometer that disperses the radiation onto a camera, which serves as the detector. The latter is determined using gas cells filled with nitrogen [23]. An FEL pulse passing through the gas ionizes it, and the resulting charge (ions or electrons) is collected and measured. The resulting signal is proportional to the pulse energy.

The measurements were taken during the preparation of FEL-1 for a user scientific program. The electron beam and FEL were characterized and optimized prior to the experimental R_{56} scans.
The experiment included three scans with increasing intensity of the laser heater that is used to effectively change the electron beam energy spread σ_E [17]. This was followed by a scan with reduced seed laser energy E_s, effectively reducing the seed laser power P. Table 3 provides an overview of the parameters that were varied in the respective scan.

Table 3: Parameters varied in the experimental R_{56} scans and their values as well as the effectively changed model input parameter.

Scan number	1	2	3	4
Changed parameter	Laser heater energy			E_s
Parameter value	16.3 μJ	21.1 μJ	62.6 μJ	15 μJ
Effectively changed parameter	σ_E			E_s

The remaining electron beam and seed laser parameters were kept constant throughout the experimental scans according to the rightmost column in Table 1, except for the seed laser wavelength, which was set to $\lambda_s = 250$ nm. As in the simulation study, these values were also used as input parameters in the model implementation for direct comparison. Note that instead of the pulse duration τ_0 the bandwidth $\Delta\lambda_s$ of the seed laser was measured, assuming a Gaussian Fourier-limited pulse.
In the experiment, these values naturally contain some uncertainties as the quantities have to be measured and cannot be set with perfect precision. Further, the beam size σ_x is not constant along the FEL setup, but oscillates, and hence an average of the value at different measurement points was taken. The measurements included placing screens on axis of the beam path at seven points along the FEL. The resulting signal was then detected by a camera, and an average over the measurements was found.

To analyze the measurements, the same procedure was used for fitting the model to the experimental data as described for the simulation outputs, with one exception: Instead of the seed laser power P, the seed laser waist w_s was chosen as fitting parameter, as w_s cannot be accurately measured by experiment in contrast to P. Nevertheless, these parameters are closely related for the purpose at hand, considering that multiplying P by a factor x gives the same change in FEL intensity as dividing w_s by $\sqrt{x}$.

4 Results and Discussion

4.1 Simulations

Before proceeding to the quantitative analysis, spectrum intensities of both simulation and the model are presented in Figure 5 to illustrate that the model captures the essential FEL behavior qualitatively. Shown are the globally normalized spectral intensities as 2D maps versus wavelength and R_{56} as predicted by the simulation (uppermost panel) and the model (cenral panel). As a representative case the center point of the simulations with all three analyzed parameters at nominal values is displayed ($\sigma_E = 60$ keV, $I = 700$ A, $P = 100$ MW). The bottom panel shows the extracted position of the peak wavelengths as given by the simulation and the model outputs, respectively.

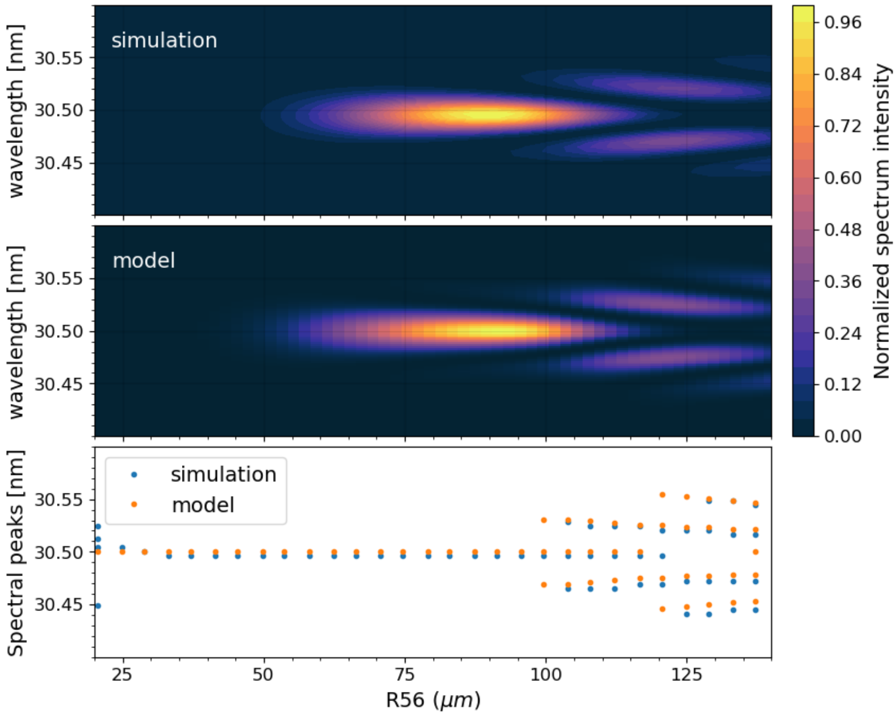

Figure 5: Normalized FEL spectrum intensities as predicted by *Genesis-1.3* simulation and the model, respectively. Shown is the central point in parameter space (σ_E = 60 keV, I = 700 A, P = 100 MW). The lower panel shows the extracted peak wavelengths from both spectra.

The shown main spectral features agree under visual inspection. It is evident that the model correctly reproduces the spectral splitting, which results from overbunching at larger R_{56}. Nevertheless, a minimal difference in peak wavelengths and symmetry emerges. In general, the peak wavelengths are slightly smaller in the simulation compared to the model, which becomes evident in the lower panel of Figure 5. Further, the simulation spectra are not symmetric with respect to the central wavelengths, while the model output shows perfect symmetry. This symmetry deviation originates most likely from slippage effects in the undulators, which the model does not take into account. However, these discrepancies are small.

In the following, the quantitative analysis of the model validity throughout the defined parameter space is presented as a study of energy per pulse based on the fit of the model to the simulation output. Figure 6 illustrates the respective fit of two exemplary cases, including a report of the respective input and best fit parameters, i.e. the model's prediction of the input parameters. The simulated energy per pulse (blue) is plotted together with the best fit of the model (orange). Additionally, the model output as found for the exact parameters used in the simulations is depicted (green). Figure 6a shows the fit of the parameter space center point for reference. Figure 6b represents an exemplary case that results only in a single peak pulse energy. As has been mentioned in section 2.2 a unique determination of beam energy spread, current and seed laser power upon fit is only possible given the existence of a second peak, whereas a single peak may be a projection of more than one input parameter combinations. Hence, the resulting predictions in these cases depend on the initial guess of the fit, in the case of this study the simulation input parameters. However, to retrieve more reliable results in these cases, a careful study using a second observable such as the spectrum intensity should be considered.

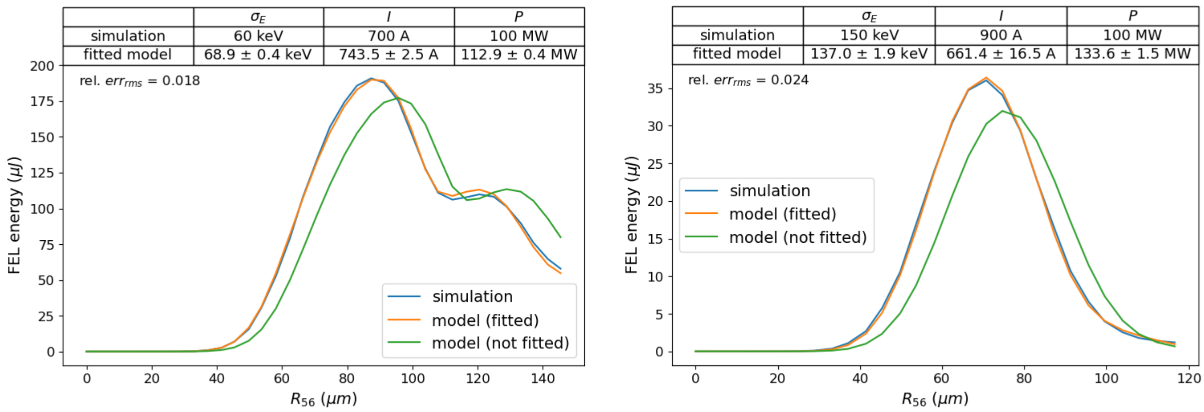

(a) (b)

Figure 6: FEL energy per pulse as predicted by simulation (blue) and the model (green) for the reported simulation input parameters. The fitted model (orange) and the parameters as predicted by the model upon fit are reported, as is the relative rms error of the shown best fit. The errors in the parameter predictions correspond to the uncertainties of the fit. Panel (a) displays the nominal central point in parameter space, while panel (b) shows the extreme case of largest input values for all three parameters, as reported in the table above the respective figure.

From inspection of the fits of all 125 investigated parameter combinations, it becomes evident that the model's capability to reproduce the simulation output, quantified by the relative rms error err_{rms}, depends on the maximum FEL pulse energy produced by the given electron beam and seed laser settings. In conclusion, the model is not capable of correctly reproducing the simulation for very low FEL pulse energies. Careful consideration of err_{rms} suggests a restriction of the model's validity to pulse energies higher than a threshold of 15 μJ. Hence, these cases are excluded from further analysis. Upon closer inspection, the most problematic cases, i.e. with either very low pulse energy or an ambiguity in fitting (as in Figure 6b), occur for parameter combinations that lead to a (very) low initial bunching. In *Genesis-1.3*, low initial bunching can lead to a startup from shot noise, i.e. a SASE dominated process. This cannot be predicted by the model.

With the goal of defining regions of validity in parameter space, the deviations $\Delta p = p_{\text{fit}} - p_{\text{sim}}$ are analyzed in detail below, following the steps presented in Section 3.3. The results are organized by parameter deviations $\Delta\sigma_E$, ΔI, ΔP. Due to the definition of "validity" of the model predictions, the absolute deviations of σ_E were analyzed, while the relative deviations of the other two parameters were investigated.

The baseline analysis for $\Delta\sigma_E$, shown in Figure 16 in Appendix C, reveals that the model gives the most accurate prediction of the beam energy spread at maximal σ_E and minimum seed laser power P. The latter has the strongest absolute effect on the total deviation, while the current I introduced only small fluctuations. These can be regarded negligible when taking the error introduced by the fitting into account.

However, these results are not automatically valid across the full parameter space. The 2D map in Figure 7 depicts the average absolute deviation of the energy spread $\langle\Delta\sigma_E\rangle$ at each point (P, I) in parameter space, revealing spatial patterns of parameter dependence. Note that all maps shown in this section only display the respective deviations at single points, as indicated on the axes, and do not give information about the intermediate regions between these points!

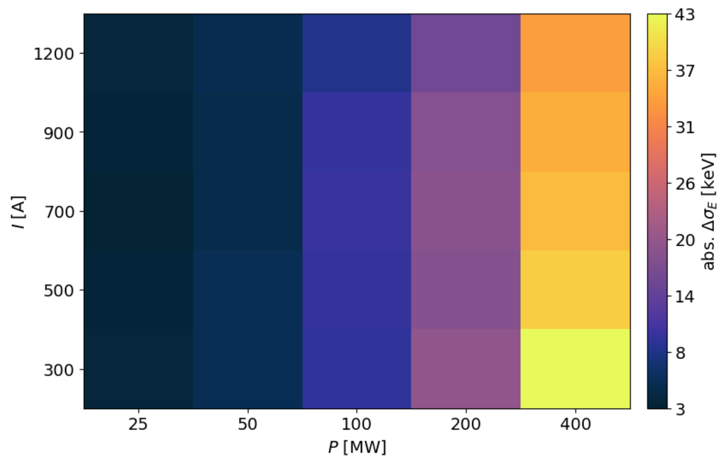

Figure 7: Average absolute deviation of the predicted energy spread by the model from simulation, $\langle\Delta\sigma_E\rangle$, evaluated at each point (P, I). Note that each rectangle refers to the deviation at a single point, as indicated by the ticks on the axes, and not to the intermediate regions!

Under inspection of Figure 7, the strong increase of $\langle\Delta\sigma_E\rangle$ with seed laser power can indeed be observed throughout the full parameter space. Furthermore, the two-dimensional analysis confirms the independence of $\langle\Delta\sigma_E\rangle$ of the current I. Nevertheless, with growing seed laser power P, low currents are less slightly favored, which implies the possibility of a coupling of P and I in their effect on $\langle\Delta\sigma_E\rangle$ for high P. However, this result could also be an artifact of the coarse grid (P, I).

Further investigation of possible coupling effects requires a discussion of the results of the sensitivity analysis. Figure 8a illustrates the effect of I on the deviation $\Delta\sigma_E$ vs. σ_E, averaged over all P. The three curves resulting from higher I mostly overlap when the error introduced by the fit is taken into account. Higher currents seem to be slightly more ideal, but the errors prevent a reliable conclusion. Only the curve for I =300 A clearly deviates from this trend when the error bars are considered. On the contrary, the curves of Figure 8b which in turn shows $\Delta\sigma_E$ for each P, averaged over all I, are distinctly separated.

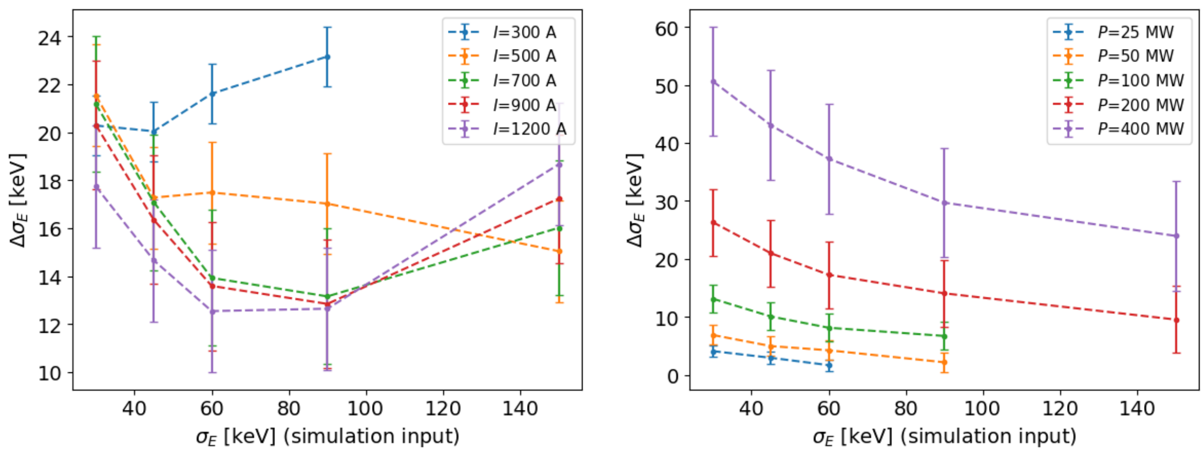

(a) (b)

Figure 8: Absolute deviations $\Delta\sigma_E$ as a function of σ_E for (a) each I and (b) each P. Each data point was found as the average $\Delta\sigma_E$ at the given P (I) over all values of I (P). Points in parameter space were excluded where the resulting FEL pulse energy was below 15 μJ, leading to fewer than five data points for some lines. The error bars denote $\pm 1\sigma$.

The overlapping curves of Figure 8a clearly confirm the independence of $\Delta\sigma_E$ of the current as found in the baseline analysis. However, this seems not to be true at low current ($I = 300$ A). In agreement with the earlier findings illustrated by Figure 7, low currents are not favored when averaged over all values of seed laser power.
Interestingly, at high energy spread ($\sigma_E = 150$ keV) a reversed dependence of $\Delta\sigma_E$ on the current amplitude emerges, contradicting earlier observations. This suggests either a more complex coupling pattern of I and σ_E in their effect on $\Delta\sigma_E$ or a dominating role of other mechanisms in this parameter space region. At any rate, the effect is small considering the error bars and cannot be determined with certainty.

The distinctly separated curves of Figure 8b illustrate the strong effect of P on $\Delta\sigma_E$ in agreement with the earlier findings. Since individual lines appear mostly parallel, P and σ_E seem to be additively coupled in their effect on $\Delta\sigma_E$. For high seed power ($P \geq 200$ MW), the overestimate in σ_E is nearly 10 times as large as for $P = 25$ MW.

In summary, the detailed analysis of $\Delta\sigma_E$ reveals a strong dependence on the seed laser power P throughout the full parameter space. This is most likely due to the fact that with increasing seed laser power the effective dispersive strength R_{56} of the modulator changes. However, this parameter is treated as a constant in the model, which explains the especially large deviations of the model's predictions of σ_E for large P. Further, the radiator also bears an effective dispersive strength that is modified by the seed laser power. This radiator-R_{56} has been completely neglected in this study and probably gives rise to additional deviations in the model's predictions. Moreover, $\Delta\sigma_E$ is especially large for the combination of large P and small σ_E. A possible explanation is the strong initial bunching resulting from this parameter combination, which in turn results in stronger initial coherent emission in the radiator. Starting the FEL process with a higher initial bunching leads to earlier saturation because the beam is already more strongly modulated at the radiator entrance. The closer to the saturation regime, the more relevant the additional energy spread and energy loss generated during the FEL interaction in the radiator become. These effects lead to a progressive detuning from the resonance condition in the radiator (cf. Eq. 2), which is not yet included in the model. Instead, the model assumes a constant λ_r along the entire radiator and does not account for the evolution of the electron beam energy. Since *Genesis-1.3* includes these effects, the deviation is especially large for parameter combinations resulting in an FEL power close to or at saturation. However, the deviation is still reasonable for a seed laser in the standard range ($P \approx 100$ MW).

The second main finding of the analysis of $\Delta\sigma_E$ is the influence of low current, in contrast to a lack of evidence of any relevant effect at other current amplitudes. This can be explained by the increasing number of invalid data points (FEL pulse energy < 15 μJ) with σ_E for lower current values. The combination of a low current and a high energy spread of the electron beam lead to a small bunching amplitude and consequently a weak FEL output. Only in combination with a higher seed laser power a strong enough FEL output is generated. However, as discussed above high seed laser power introduces a large error in the prediction of σ_E by the model. As the number of valid data points at low current decreases with increasing σ_E, the weight of the high power cases increases, and consequently does $\Delta\sigma_E$. In conclusion, the current does not have a significant effect on the accuracy of the predicted beam energy spread.

Analogously to above follows the analysis of the deviation of the model's prediction of the current from the simulation input, ΔI. The baseline analysis reveals that minimal ΔI is achieved at large σ_E and low P. Moreover, a low I is beneficial. An overview of these findings is given by Figure 17 in Appendix C.

Another key-finding emerges upon inspection of the 2D map in Figure 9, which shows the average deviation of the current $\langle \Delta I \rangle$ at each point (P, σ_E). The white area apparent at high energy spread and low seed laser power indicates the absence of valid data points in this parameter space region, i.e. no parameter combination resulting in a FEL energy greater than 15 μJ. This map further confirms a strong influence of the seed laser power on $\langle \Delta I \rangle$, analogously to Figure 7. Additionally, the influence of the beam energy spread follows the predictions from the baseline, as lower energy spread reduces $\langle \Delta I \rangle$. In summary, the results of the baseline analysis are applicable to the whole parameter space, except for the region that has been classified as invalid.

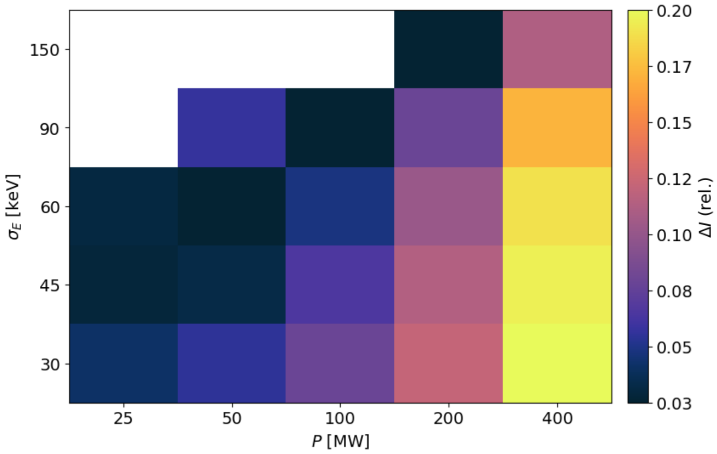

Figure 9: Average relative deviation of the predicted energy spread by the model from simulation, $\langle \Delta I \rangle$, evaluated at each point (P, σ_E).

Lastly, the sensitivity of ΔI is investigated under variation of both P and σ_E, respectively. Figure 10a, which gives one curve for each σ_E on ΔI, averaged over all values of seed laser power, shows multiple intersections of non-parallel curves. In contrast, the individual curves of ΔI found for each P as an average over all beam energy spreads, as shown in Figure 10b, are mostly separated and in many sections parallel to each other.

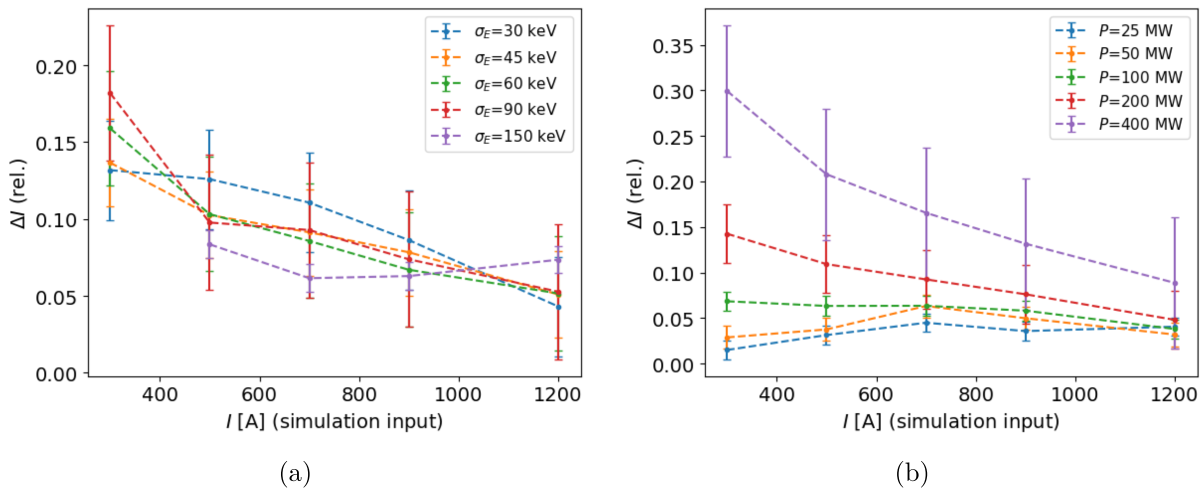

Figure 10: Relative deviations $\Delta I = (I_{\text{fit}} - I_{\text{sim}})/I_{\text{sim}}$ as a function of I for (a) each σ_E and (b) each P. Each data point was found as the average ΔI at the given σ_E (P) over all values of P (σ_E). The error bars denote $\pm 1\sigma$.

Inspecting the curves in Figure 10a does not allow for definite conclusions due to the widely overlapping error bars. The baseline observation of large σ_E reducing ΔI seems to be confirmed at intermediate currents only, while the relation is reversed at low ($I = 300$ A) and high current ($I = 1200$ A). However, the large variations for different seed powers P resulting in the displayed errors prevent an unambiguous interpretation.

The distinct separation of the individual curves in Figure 10b once more confirms that the seed laser power has a similarly strong effect on ΔI as has been shown for $\Delta\sigma_E$. Following the baseline analysis, low P is in general more optimal and the absolute deviation ΔI introduced by P is expected to be especially large for high powers ($P > 100$ MW). The observation of overall nearly parallel curves (under exemption of $P = 400$ MW) suggests an additive coupling between P and I, i.e. an independent effect of both parameters on ΔI.

Upon summarizing the main findings of the analysis of ΔI, it is obvious that the seed laser power P again has the strongest effect on the accuracy of the model's prediction throughout the full parameter space. This originates from the same effects that have been discussed earlier for $\Delta\sigma_E$: increasing seed laser power in general modifies the effective R_{56} of the undulators, and moreover leads to the FEL power approaching saturation, which are both effects that the model does not take into account. These effects are driven by the power and hence affect both $\Delta\sigma_E$ as well as ΔI.

Compiling the findings of the effect of σ_E on ΔI showed some unexpected behavior at very low and very high currents. At low current, a low beam energy spread seems to be favored, which could be explained by the combination of low current and large energy spread leading to reduced initial bunching and consequently invalid data points due to low FEL output, as discussed above. At high current, the case of $\sigma_E = 150$ keV results in the maximum ΔI, contrary to the baseline analysis and the intermediate current region. This is again an artifact of a low number of valid data points giving a greater weight for the high current case: for large energy spread, the initial bunching is small at low seed power, even for high current. Hence, these cases result in a low FEL output, reducing the number of data points. Only high powers yield valid points, but these introduce a larger error in the predictions due to the above reasons.
However, due to large fluctuations introduced by the seed laser power, no unambiguous conclusions can be drawn in this case.

Finally, the deviation of the seed laser power as predicted by the model from the simulation input, ΔP is evaluated.
The baseline analysis of this case, as illustrated by Figure 18 in Appendix C, shows that the prediction of the seed laser power is optimized for low I and P, respectively. Interestingly, it is fully independent of σ_E.

Figure 11 displays the average seed laser power deviation $\langle\Delta P\rangle$ at each (σ_E, I). This 2D map confirms that the baseline finding of an optimized $\langle\Delta P\rangle$ at low current is applicable to the full parameter space. Moreover, it reveals that the combination of high energy spread and low current ($\sigma_E = 150$ keV, $I = 300$ A) leads to no valid model predictions due to an FEL energy lower than 15 μJ. However, Figure 11 implies that the effect of the energy spread on $\langle\Delta P\rangle$ is negligible only at low σ_E and not in general. Once σ_E increases from 90 keV to 150 keV, a dependence becomes visible.

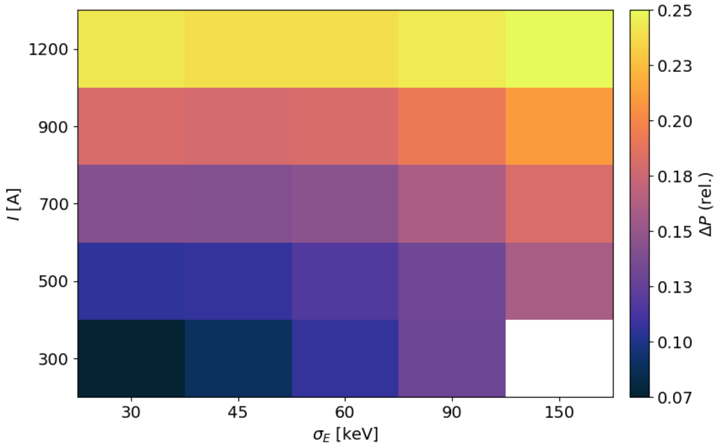

Figure 11: Average relative deviation of the predicted seed laser power by the model from simulation, $\langle \Delta P \rangle$, evaluated at each point (σ_E, I).

This result is confirmed by Figure 12b, which shows ΔP as a function of seed laser power P for each σ_E, averaged over all values of I. The overlapping lines indicate an independence of ΔP on σ_E. Only for $\sigma_E = 150$ keV and for low seed powers an effect becomes visible as ΔP increases, which suggests a different dominating mechanism in this case. However, it should be mentioned that at low seed powers, the absolute deviation is still small. More generally, Figure 12 reveals a strong sensitivity of ΔP to P.

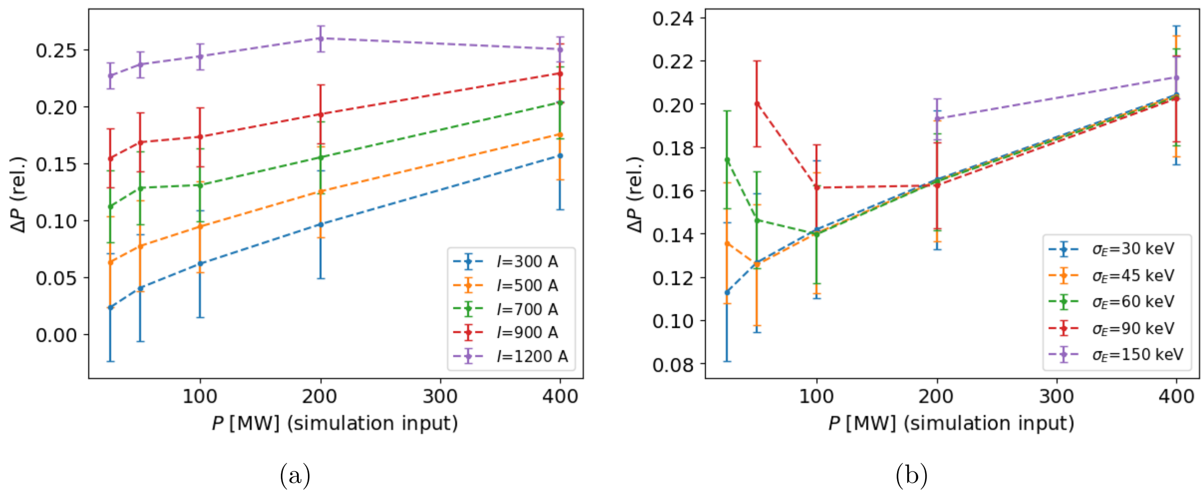

Figure 12: Relative deviations $\Delta P = (P_{\text{fit}} - P_{\text{sim}})/P_{\text{sim}}$ as a function of P for (a) each I and (b) each σ_E. Each data point was found as the average ΔP at the given I (σ_E) over all values of σ_E (I). The error bars denote $\pm 1\sigma$.

Figure 12a shows ΔP for each I, averaged over all values of σ_E. In this case, the curves are clearly separated, confirming the discussed dependence of ΔP on the current I. The similarly curved line shapes suggest an additive coupling between I and P in their effect on ΔP.

To sum up the main results found from analyzing ΔP, again the strong effect of the seed power stands out. From this, it can be concluded that the underlying reasons discussed above equally effect $\Delta \sigma_E$, ΔI and ΔP.
While only large σ_E has a some effect on ΔP, the peak current does have a relevant influence. That is possibly due to the current having a direct effect on the gain length, such that increas-

ing currents lead to saturation faster for a given P. In contrast, σ_E influences the bunching amplitude, which has a weaker total effect on the power gain across normal operating ranges than the peak current.

Finally, the valid region of the parameter space can be defined based on the definition of validity introduced in Section 3.3 under consideration of the found deviations in the model's predictions. The resulting classification of each point in the defined parameter space is shown in Figure 13. Black points are classified invalid due to weak FEL output (excluded from the analysis), while red points yield invalid model predictions due to high inaccuracy in one or more parameters. Light green points indicate valid points, but low accuracy, while dark green points mark the parameter combinations yielding highly accurate model predictions.
Figure 13 suggests entire regions in parameter space that lead to either valid or invalid model predictions. The black points referring to low FEL pulse energy are concentrated at low seed power, covering a triangular area in the $\sigma_E - I$ plane, accumulating at high energy spread. The high inaccuracy region shown in red covers nearly exclusively all points with a seed power greater than or equal to 200 MW. However, the combination of $P = 200$ MW with intermediate energy spread and current does lead to valid points with intermediate accuracy (light green). In general, the valid points accumulate at low energy spread up to approximately 60 keV, seed power less or equal to 100 MW, but no restriction in current. However, currents greater or equal to 700 A lead to a higher inaccuracy of the predictions, illustrated by the light green cloud in this parameter space region.

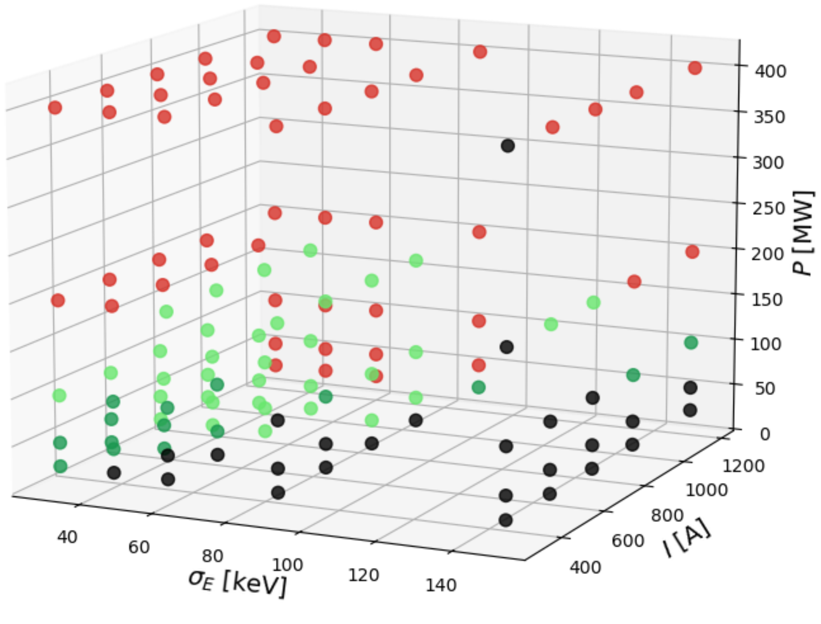

Figure 13: Validity of the model predictions at the evaluated points in the defined parameter space. Black points are invalid due to weak FEL output, while red points mark low accuracy in one or more parameter predictions ($\Delta\sigma_E > 20$ keV, $\Delta I > 20\%$, $\Delta P > 20\%$). Light green classifies valid input points, that yield intermediate deviations upon model predictions ($10 < \Delta\sigma_E \leq 20$ keV, $10\% < \Delta I \leq 20\%$, $10\% < \Delta P \leq 20\%$). Dark green marks valid points with high accuracy in all three parameters ($\Delta\sigma_E \leq 10$ keV, $\Delta I \leq 10\%$, $\Delta P \leq 10\%$).

4.2 Experimental Data

Similarly to the evaluation of the simulations, the spectral intensities measured during the experimental R_{56} scans were compared to the model output for equal beam and seed laser settings. Figure 14 serves to illustrate that the model again captures the essential spectral FEL behavior qualitatively by showing the FEL spectrum measured in scan (4) as an example.

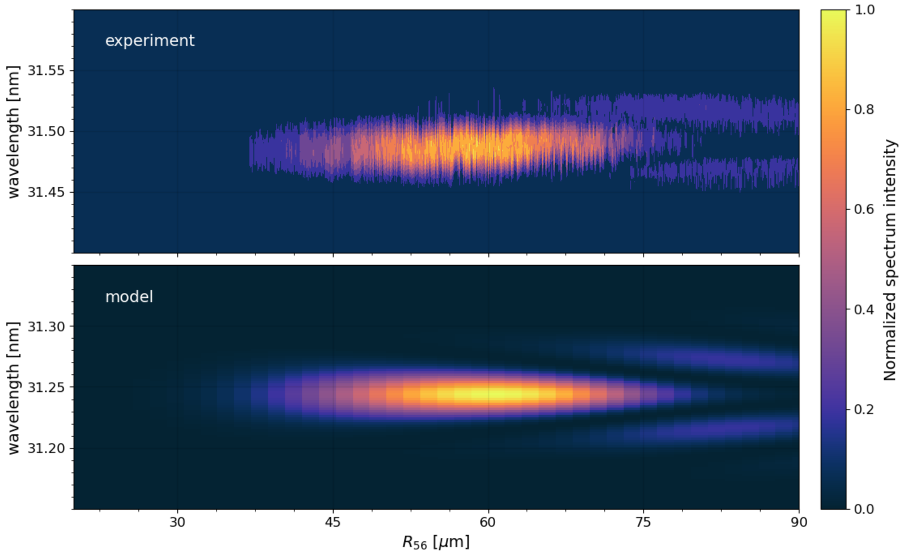

Figure 14: FEL spectrum intensity measured in scan (4). The lower panel shows the spectrum predicted by the model using the input parameters found from the fit to the pulse energy of this scan ($\sigma_E = 90 \pm 1$ keV, $I = 587 \pm 3$ A, $w_s = 713 \pm 4$ μm).

The deviations between the simulated and experimentally measured FEL spectra are evident and arise primarily from imperfect calibration of the measurement devices, their finite resolution, and shot-to-shot variations in beam parameters that may not be fully captured in the simulations.
Again, the model reproduces the spectral splitting at higher R_{56}. Moreover, the spectral intensities per R_{56} coincide in general. The blueshift of the peak wavelengths predicted by the model is an artifact of a significant miscalibration of the used spectrometer.

To investigate the model's ability to predict the energy spread of the electron beam, the beam peak current, and the waist of the seed laser under real conditions, the model output of FEL pulse energy was fitted to the respective measurement as a function of σ_E, I and w_s, returning the best fit parameters.

Unlike in simulations, where the input values are known exactly, the three parameters under investigation cannot be easily measured in an experiment, and hence the values predicted by the model are qualitatively compared with expectations.
Scans (1) to (3) investigated the effect of increasing the laser heater intensity. The measurements of the FEL pulse energy and the respective fits of the model for scan (1) and (3) are displayed in Figure 15. Figure 15a shows the case with a laser heater energy of 16.3 μJ, while Figure 15b plots the data that resulted from an energy of 62.6 μJ. The red scatter plot shows the mean energy measured for the respective bin. The blue line connects the measurements, while the orange plot shows the resulting best fit of the model.

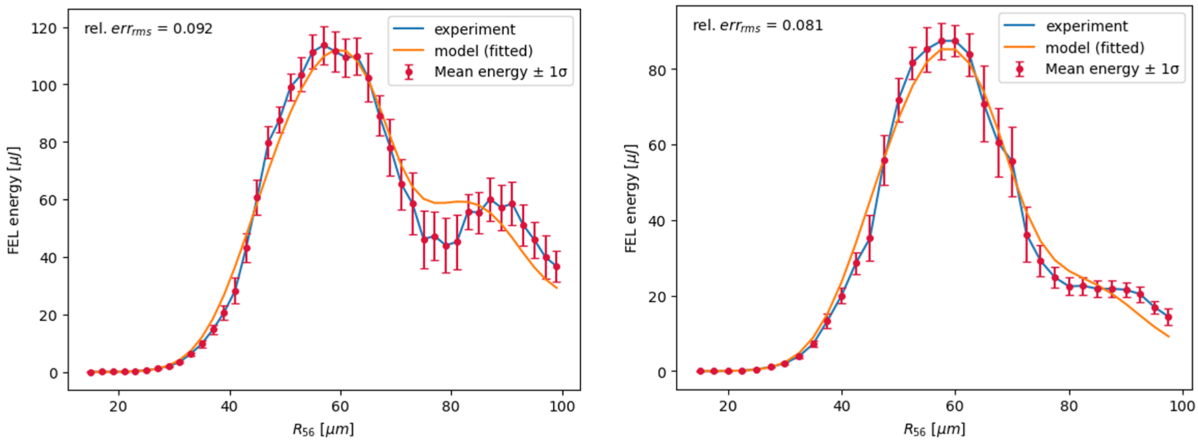

(a) (b)

Figure 15: Measurements of FEL pulse energy versus R_{56} of the chicane for a laser heater energy of (a) 16.3 μJ and (b) 62.6 μJ, including the best fit of the model to the data and the relative rms error. The fit yielded the parameter values (a) $\sigma_E = 101 \pm 3$ keV, $I = 616 \pm 4$ A, $w_s = 693 \pm 5$ μm and (b) $\sigma_E = 131 \pm 2$ keV, $I = 653 \pm 4$ A, $w_s = 712 \pm 4$ μm.

Increasing the laser heater's energy was expected to effectively increase the beam's energy spread. Figure 15 illustrates this effect: a decrease in the ratio of the pulse energy of the first to the second peak is characteristic of an increase in energy spread. This is a result of the decreased bunching for a higher σ_E, which in turn yields a stronger suppression at larger R_{56}, i.e. stronger damping. This trend was correctly predicted by the model upon fit to the measurements, as shown in Table 4, which reports the best fit parameters for each scan.

Table 4: Parameter values predicted by the HGHG model upon fit to the measured FEL pulse energies of the respective scan.

Scan number	σ_E	I	w_s
1	101 ± 3 keV	616 ± 4 A	693 ± 5 μm
2	104 ± 2 keV	626 ± 4 A	697 ± 4 μm
3	131 ± 2 keV	653 ± 4 A	712 ± 4 μm
4	90 ± 1 keV	587 ± 3 A	713 ± 4 μm

As discussed, it has been shown that the model's predictions of the three investigated parameters depend on the R_{56} values of the first and second peaks, as well as the ratio of the FEL energy at these peaks. Figure 15 illustrates that within the accuracy of the measurement the model is capable of reproducing these points of interest correctly. However, the predictions of the current and the seed waist also showed some increase, contrary to the assumptions that these parameters remained constant during the measurements. This overestimation is likely due to instrumental effects, as the detector used to measure the FEL pulse energy might react non-linearly. This would directly affect the respective measurement result, which in turn modifies the model's parameter predictions when fitted. Another source of error is introduced by the estimate of the electron beam size that was used as input parameter in the model. This parameter is directly related to the transverse phase space properties of the electron beam. The used diagnostic is destructive, meaning that the measured beam does not exactly correspond to the one used in the subsequent scans. Further, it does not resolve the temporal axis of the bunch, i.e. the screen detects a common transverse beam size for all temporal slices, which could lead to an overestimate. Additionally, the beam size in a real FEL oscillates along the FEL due to (de-)focusing, typically by quadrupole magnets, but is kept constant in the model, using the average of the measured values. In any case, it is important to note that these changes in the predictions of the beam current and the seed waist do not affect the determined energy spread.

In scan (4), conducted with reduced seed laser energy, a decrease in only the FEL pulse energy was expected, while σ_E, I, and w_s should remain unchanged. The former was indeed observed, as the maximum pulse energy decreased from around 110 μJ to approximately 95 μJ. Comparing to scan (1), Table 4 reports negligible changes in I and w_s, which might be due to noise in the measurements. The change in σ_E is around 10 keV, which is means a good approximation when compared to the defined validity ranges.

5 Conclusion and Outlook

This study explored the behavior of a simplified model for a HGHG seeded FEL throughout a defined parameter space with the ultimate goal of identifying areas of validity and determining the accuracy of the model's predictions in these regions. "Validity" was defined based on the deviation of the model's predictions for the electron beam energy spread σ_E, the beam peak current I and the seed laser power P. These findings are especially relevant for the possible application of the model as a tool to determine these quantities in real FEL applications, as they are not easily measured experimentally. Hence, it is of outmost importance to assign such predictions with an accuracy in order to achieve reliable results.

It has been shown that the model is able to predict all three of σ_E, I and P with high accuracy only in a limited region of parameter space. This region is confined close to the origin, where all three parameters attain low values. However, real applications are not restricted to this rather small parameter space region and hence extensions of the model should be considered to guarantee reliable predictions.
Further, it became clear that seed laser powers greater than or equal to 200 MW lead to unreliable model predictions in most cases. These were most likely due to a strong initial bunching resulting from these conditions, which lead to the system approaching saturation in the radiator. Additionally, a change in the effective R_{56} of the undulators in the setup is likely under these circumstances. The saturation regime is not easy to model due to a time-dependent change in the resonance condition. This effect is not yet included in the model, but planned as a future extension. However, this will require a deeper study of the process accompanied by careful comparison to a large number of simulations.
Moreover, the model currently considers only a constant effective R_{56} of the modulator and completely ignores the dispersion introduced by the radiator. Hence, it might be of merit to further investigate if the model can be improved in this direction.

Additionally, the observation emerged that the deviation of the model predictions increases with peak current even in parameter space regions defined by both low energy spread and power. To further investigate the model's reliability in higher current regions, a setup using less undulators in the radiator could be considered. As a higher peak current increases the FEL parameter ρ_{FEL} and shortens the gain length L_{g0}, saturation is also approached at an earlier point in the radiator in this case. A shorter undulator would hence prevent the system from growing close to saturation.
Finally, it was demonstrated that the model is not capable of correctly reproducing a (very) low FEL pulse energy. Hence, invalid predictions accumulate as the energy spread increases, especially in combination with low seed laser powers.

In general, it must be mentioned that this study was not an exhaustive analysis of the model reliability. The electron beam as well as the seed laser are characterized by a large number of

parameters that were all but three kept constant in this approach. To determine more potential improvements of the model, the analysis could be expanded to cover more of these parameters. Further, the grid of evaluated points in the defined parameter space was coarse. To correctly interpolate the intermediate regions, a larger number of grid points might be considered. However, this study has proved to be a useful approach to investigate the reliability of the model in a limited parameter space. Based on the approach and the results of this work, an automatic procedure to evaluate a larger set of configurations could now be implemented to expand the model analysis.
Similarly, using a different fitting mechanism could be beneficial. In this study, only the three investigated parameters were fitted, while a fit of a function of all beam and seed laser input parameters might lead to different results, as other coupling mechanisms might evolve.

In conclusion, the theoretical model investigated in this study is a powerful tool to both predict FEL performance and to extract beam and seed laser parameters from measurements of the FEL pulse energy. The successful agreement between the model and the experimental data, along with the consistent qualitative response of the parameter predictions to varied conditions, supports the future use of these methods in control room operations to guide electron beam and both FEL characterization and optimization. Further extensions of this theory will not only result in more reliable model predictions, but also enable a better understanding of the underlying FEL processes by implementing them into a theoretical construct. In the long term, this can contribute to more efficient optimization of operating conditions and enhanced control of FEL output for a wide range of experimental applications.

References

[1] E. Allaria et al. "Accurate Measurements of Slice Electron Beam Parameters at the Undulator in Seeded Free-Electron Lasers". In: *Journal of Synchrotron Radiation* 32.1 (2024), pp. 72–81. DOI: `10.1107/S1600577524011585`.

[2] E. Allaria et al. "Highly coherent and stable pulses from the FERMI seeded free-electron laser in the extreme ultraviolet". In: *Nature Photonics* 6.10 (2012), pp. 699–704. DOI: `10.1038/NPHOTON.2012.233`.

[3] R. Bonifacio, C. Pellegrini, and L.M. Narducci. "Collective instabilities and high-gain regime in a free electron laser". In: *Optics Communications* 50.6 (1984), pp. 373–378. DOI: `10.1016/0030-4018(84)90105-6`.

[4] G. Dattoli et al. "An Introduction to the Theory of Free Electron Lasers". In: *CAS CERN Accelerator School - Synchrotron Radiation and Free Electron Lasers, Chester College, Chester, 1989*. Ed. by S. Turner. CERN European Organization for Nuclear Research, 1990, pp. 254–286. ISBN: 92-9083-022-0.

[5] P. Emma et al. "First lasing and operation of an ångstrom-wavelength free-electron laser". In: *Nature Photonics* 4.9 (2010), pp. 641–647. DOI: `10.1038/nphoton.2010.176`.

[6] D. Gauthier et al. "Spectrotemporal Shaping of Seeded Free-Electron Laser Pulses". In: *Physical Review Letters* 115.11 (2015), p. 114801. DOI: `10.1103/PhysRevLett.115.114801`.

[7] Luca Giannessi. "Seeding and Harmonic Generation in Free-Electron Lasers." In: *Synchrotron Light Sources & Free-Electron Lasers* (2016), pp. 195–223. DOI: `10.1007/978-3-319-14394-1_3`.

[8] E. Hemsing, G. Stupakov, and D. Xiang. "Beam by Design: Laser Manipulation of Electrons in Modern Accelerators". In: *Reviews of Modern Physics* 86.3 (2014), pp. 897–941. DOI: `10.1103/RevModPhys.86.897`.

[9] A. M. Kondratenko and E. L. Saldin. "Generation of coherent radiation by a relativistic-electron beam in an ondulator". In: *Particle Accelerators* 10 (1980), pp. 207–216.

[10] S.Y. Lee. *Accelerator Physics*. World Scientific Publishing, 2019. ISBN: 78-981-3274-69-3.

[11] J.M.J. Madey. "Stimulated emission of Bremsstrahlung in a periodic magnetic field". In: *Journal of Applied Physics* 42.5 (1971), pp. 1906–19013. DOI: `10.1063/1.1660466`.

[12] B.W.J. McNeil and N.R. Thompson. "X-ray Free-Electron Lasers". In: *Nature Photonics* 4.12 (2010), pp. 814–821. DOI: `10.1038/nphoton.2010.239`.

[13] F. Pannek et al. "Accurate Control of Seed and Free-Electron Laser Chirp with Bunching Spectral Analysis". In: *14th International Particle Accelerator Conference, Venice, Italy*. TUPL: Tuesday Poster Session. JACoW Publishing, 2023, pp. 1954–1957. ISBN: 978-3-95450-231-8. DOI: `10.18429/JACoW-IPAC2023-TUPL099`.

[14] S. Reiche. "GENESIS 1.3: a fully 3D time-dependent FEL simulation code". In: *Nuclear Instruments and Methods in Physics Research Section A: Accelerators Spectrometers Detectors and Associated Equipment* 429.1–3 (1999), pp. 243–248. DOI: `10.1016/S0168-9002(99)00114-X`.

[15] P. Schmüser et al. *Free-Electron Lasers in the Ultraviolet and X-Ray Regime*. Vol. 258. Springer Tracts in Modern Physics. Springer, 2014. ISBN: 978-3-319-04081-3. DOI: `10.1007/978-3-319-04081-3`.

[16] S. Schreiber and B. Faatz. "The free-electron laser FLASH." In: *High Power Laser Science Engineering* 3 (2015), N.PAG. DOI: `doi:10.1017/hpl.2015.16`.

[17] S. Spampinati et al. “Laser heater commissioning at an externally seeded free-electron laser”. In: *Physical Review Special Topics. Accelerators and Beams* 17.12 (2014), pp. 120705–120705. DOI: 10.1103/PhysRevSTAB.17.120705.

[18] H. Wiedemann. *Particle Accelerator Physics*. Graduate Texts in Physics. Springer, 2014. ISBN: 978-3-319-18316-9. DOI: 10.1007/978-3-319-18317-6.

[19] K. Wille. “Introduction to Insertion Devices”. In: *CAS CERN Accelerator School - Synchrotron Radiation and Free Electron Lasers, Grenoble, France, 1996*. Ed. by S. Turner. CERN European Organization for Nuclear Research, 1998, pp. 61–71. ISBN: 92-9083-131-6.

[20] M. Xie. “Design optimization for an X-ray free electron laser driven by SLAC linac”. In: *Proceedings Particle Accelerator Conference, Dallas, TX, USA*. 1995, pp. 183–185. DOI: 10.1109/PAC.1995.504603.

[21] M. Xie. “Exact and variational solutions of 3D eigenmodes in high gain FELs”. In: *Nuclear Instruments and Methods in Physics Research Section A: Accelerators Spectrometers Detectors and Associated Equipment* 445.1–3 (2000), pp. 59–66. DOI: 10.1016/s0168-9002(00)00114-5.

[22] L.J. Yu. “Generation of Intense UV Radiation by Subharmonically Seeded Single-Pass Free-Electron Lasers”. In: *Physical Review A* 44.8 (1991), pp. 5178–5193. DOI: 10.1103/physreva.44.5178.

[23] Marco Zangrando et al. “Recent results of PADReS, the Photon Analysis Delivery and REduction System, from the FERMI FEL commissioning and user operations.” In: *Journal of Synchrotron Radiation* 22.3 (2015), pp. 565–570. DOI: 10.1107/S1600577515004580.

6 Appendix

A Code Structure and Module Overview

The subsequent diagram illustrates the structure of the code implementation of the theoretical HGHG model.

```
HGHG_model/
|
|-- config/
|    |__ parameters.py
|
|-- core/
|    |-- builders.py
|    |-- FEL_classes.py
|    |-- FEL_functions.py
|    |__ R56_scan_model.py
|
|-- plotting/
|    |__ R56scan_plots.py
|
|-- main.py
|__ physical_constants.py
```

In the following sections, the contents of each package is described. The packages are presented in the order in which they are used during code execution.

Top-level Modules

In addition to the packages of the program, the code contains two top-level modules that serve for global execution and the definition of physical constants.

Contained modules:

- `main.py`
- `physical_constants.py`

Module descriptions:

1. `main.py`

Purpose: Entry-point of the implementation. Orchestration of the execution workflow.

2. `physical_constants.py`

Purpose: Initialization of the physical constants used by the other models according to 2018 CODATA recommended values. Examples are the speed of light and the elementary charge.

Configuration Package

The configuration package contains all user-defined parameters and global settings.

Contained module:

- `parameters.py`

Module descriptions:

1. `parameters.py`

Purpose: Initialization of the input parameters.
Function:

- `default_parameters` – Returns a dictionary of default initial parameters, which may be adapted by the user.

An exhaustive parameter dictionary is given by Table 5.

Table 5: Input parameters defined in `parameters.py` that are used in the code implementation of the theoretical HGHG model.

Variable name	Type	Description	Unit
`E0`	float	nominal electron beam energy	GeV
`sigma_E`	float	rms energy spread of the electron beam	keV
`current`	float	electron beam current	A
`emittance_n`	float	normalized emittance of the beam	mm · mrad
`beamsize`	float	transverse size of the electron beam	μm
`lambda_seed`	float	wavelength of the seed laser	nm
`bandwidth_seed`	float	bandwidth of the seed laser	nm
`tau_0`	float	pulse duration of the seed laser	fs
`energy_seed`	float	energy of the seed laser	μJ
`power_seed`	float	peak power of the seed laser	MW
`waist_seed`	float	waist of the seed laser	μm
`harmonic`	int	desired harmonic of the seed laser to be amplified in the radiator	-
`n_rad`	int	number of undulators used in the radiator	-
`pol_rad_circ`	Boolean	`True` for circularly polarized undulators, `False` for linearly polarized undulators	-
`rad_effic`	float	factor between 0 and 1 to scale the radiator length	-
`R56_exp`	ndarray	array of R_{56} values to be scanned	μm
`time_range_factor`	float	factor to determine the resolution in time	-
`plot_method`	string	option to select the desired output plots	-
`normalize`	Boolean	option to globally normalize the spectral intensity plots	-
`norm_each`	Boolean	option to normalize the spectral intensity plots per R_{56} value	-

Core Package

The core package contains the main functionality, including electron beam, laser, and FEL modeling and the implementation of the theoretical model.

Contained Modules:

- `builders.py`
- `FEL_classes.py`
- `FEL_functions.py`
- `R56_scan_model.py`

Module descriptions:

1. `builders.py`

Purpose: Construction of simulation objects, including the electron beam, the seed laser, the modulator, and the radiator.
Function:

- `build_setup` – Initializes the instances listed above from the input parameters from `config/`, using the methods of the respective classes from `FEL_classes.py` and some functions from `FEL_functions.py`.

2. `FEL_classes.py`

Purpose: Equipping each object with the relevant properties and methods.
Classes:

- `ElectronBeam` – Defines electron beam properties, such as nominal energy, energy spread and beam current. Includes methods to find the beam profile corresponding to a given time array, and to find the β function.
- `HGHGsetup` – Defines the HGHG setup. This includes the energy modulation amplitude, the dispersive strength of the chicane and the desired harmonic number.
- `Laser` – Defines the properties of the seed laser, such as wavelength, bandwidth and energy. Includes methods to find the peak power for a Gaussian profile, to set the bandwidth from the pulse duration for a Fourier-limited pulse, and to set the GDD. Further, methods to find the Gaussian envelope for the intensity, and to compute the phase are established.
- `Undulator` – Defines the undulator period, length, strength and polarization. Includes methods to find the number of periods and the undulator parameter K.

3. `FEL_functions.py`

Purpose: Definition of helper functions needed in `builders.py` and `R56_scan_model.py`.
Functions:

- `calc_a_from_seedpower` – Calculates the energy modulation amplitude produced by the seed laser.
- `def calc_energyspread_from_A` – Calculates the electron beam energy spread for a given energy modulation amplitude.
- `calc_resonant_K0` - Calculates the resonant undulator parameter K such that electron beam and seed laser wavelength satisfy the resonance condition.

- calc_undulator_R56 – Calculates the dispersive strength of an undulator.
- integrate_lower_upper_sum – Integrates an array by computing the average of its lower and upper sums.
- ming_xie_approximation – Approximates gain length, the Pierce parameter, electron beam power and Xiecorr according to [20, 21].

4. R56_scan_model.py

Purpose: Core of the implementation. Prediction of the FEL output according to the theoretical HGHG model.
Functions:

- bunching – Computes the bunching amplitude according to Eq. (7). Also finds and returns an array of time points depending on the input for time_range_factor in parameters.py. Performs a fast Fourier transform to find the bunching amplitude in frequency domain. Returns the spectral intensities found from the bunching factor.
- powergain – Computes the power gain in the radiator according to Eq. (11) using the gain length found by ming_xie_approximation. Further finds the saturation power using the Pierce parameter also returned by ming_xie_approximation
- bunching_powergain – Computes the spectral intensity in time domain including the power gain in the radiator. Find the intensity in frequency domain by fast Fourier transform. Further returns the FEL pulse power by integrating the spectra using integrate_lower_upper_sum.
- R56scan – Performs a scan over an array of R_{56} values, calling consecutively the bunching and bunching_powergain functions.

Visualization Package

The visualization package illustrates FEL spectra and pulse energy by plotting the outputs from the core/ package.

Contained module:

- R56scan_plots

Module description:

1. R56scan_plots.py

Purpose: Generating a variety of plots required to illustrate the model output.
Functions:

- R56scan_plot – Produces heatmaps of the FEL spectral intensities in time and frequency domain versus R_{56}, respectively. Two normalization options are provided: global normalization or normalization per R_{56} value. Further plots the FEL pulse energy as a function of R_{56}, also with an option to normalize with respect to the maximum pulse energy.
- peakfinder_plot – Finds the wavelength of any spectral peak(s) for each R_{56} value. Produces a scatterplot of the peak wavelength versus R_{56}.

B Input Files for the *Genesis-1.3*-Simulations

Example Input for Simulating the FEL Spectrum Intensity and Pulse Energy for a Single R_{56} of the Chicane

```
&setup

rootname = FERMI_FEL1_3rad_R56scan_1
lattice = FERMI_FEL1_3rad_R56scan_1.lat

beamline = FEL1_MOD

lambda0 = 2.44000e-07

gamma0 = 2.64188e+03

delz = 0.10

seed = 43617235
shotnoise = true
one4one = false
npart = 16384
nbins = 16

beam_global_stat = true
field_global_stat = true

exclude_current_output = false

&end

&time
slen = 2.00000e-04
sample=1
time=true
&end

#----------------------LASER-------------------------
#Seed Profile

&profile_gauss
label=seedprof
c0=1.00000e+08
s0=1.00000e-04
sig=1.27571e-05
&end

# input field ----------------------------------------
&field
power=@seedprof


dgrid=2.00e-3
ngrid=301
waist_size=1.05000e-03
waist_pos=1.50000e+00
&end

```

```
#-------------------ELECTRON BEAM--------------------
&beam
gamma = 2641.884
delgam = 0.059
current= 700.00
ex = 1.50000e-06
ey = 1.50000e-06
betax = 11.00
betay = 15.80
alphax = -0.450
alphay = 0.200

&end

# ====================SIMULALATION RUN==================
&track
output_step=5
&end

# ---------------------changing setup--------------------
# SECOND MODULATOR ---------------------------------------
&alter_setup
beamline = 3radFEL1
harmonic = 8
delz = 0.055
&end

# input field --------------------------------------------
&field
power=0.0
dgrid=2.00e-3
ngrid=301
waist_pos = 0.10
waist_size = 100.0E-6
&end

# ====================SIMULALATION RUN====================
&track
output_step=5
&end
```

Lattice File Used in the Simulations

```
#=============================================================
#========LAYOUT for FEL-1 before EEHG upgrade===============
#=============================================================

# Version: 2024-01-12
# Author:       Enrico Allaria
# Modified: Enrico Allaria
# Some qudrupoles length have been adapted to match the undulator period
# The layout is prepared to be modified by scripts for what concerns
# - R56
# - AW0
#==============================================================

# Lattice for FERMI FEL-1 before March 2022
```

```
#============================================================
# Used Magnet Lengths:
# Quadrupoles : QIUFEL, QFEL, 0.20 or 0.220 m adapted to match the und. period
# Dipoles     : R561, 0.150 m (R56 chicane)

# Undulators  :
#    MOD1, 3.000 m (FEL-1 modulator, 10 cm period planar)
#    RAD1.x, 2.500 m (FEL-1 radiator, 55 cm period APPLE2)
#============================================================

#============================================================
# DUMP MARKERS
#============================================================
BEAMDUMP:         MARK = {dumpbeam = 1};
FIELDDUMP:        MARK = {dumpfield = 1};
ALLDUMP:          MARK = {dumpfield = 1, dumpbeam = 1};
#============================================================

#============================================================
# FIRST MODULATOR SECTION
#============================================================
# Cell length: 5.500 m (undulator 3.000 m + chicane 2.5 m)

# Modulator 1: typically 260nm not tunable, but capable of operating also at 400 nm at
#              1.8GeV if required
#-----------------------------------------------------------
MOD_U1:   UNDULATOR = {lambdau = 0.10, nwig = 30, aw = 5.73830};

# Chicane: typically at few tens of um capable of few hundreds of um
#
#------------------------------------------------------------
MOD_D1:  DRIFT = { l = 0.200 };
MOD_C1:  CHICANE = { l = 1.3, lb = 0.15, ld = 0.35, delay = 0.00000e+00};
MOD_D2:  DRIFT = { l = 0.300 };
MOD_Q1:  QUADRUPOLE = { l = 0.2, k1= 0.705};
MOD_D3:  DRIFT = { l = 0.500 };

FEL1_MOD:LINE = {MOD_U1,MOD_D1,MOD_C1,MOD_D2,MOD_Q1,MOD_D3};

#============================================================
#============================================================
# RADIATOR 6*2.420+5*1.210
#============================================================
# Cell length: 3.630 m (undulator 2.420 m + drift 1.210 m)

# Undulator period is 55 mm, quads and drift length adjusted to be multiple of
#    the undulator period
#------------------------------------------------------------
# UNDULATOR, each seperately for tapering
RAD1_U1:  UNDULATOR = {lambdau=0.055, nwig=44, aw = 2.59114, helical=true, kx=0.5, ky=0.5};
RAD1_U2:  UNDULATOR = {lambdau=0.055, nwig=44, aw = 2.59114, helical=true, kx=0.5, ky=0.5};
RAD1_U3:  UNDULATOR = {lambdau=0.055, nwig=44, aw = 2.59114, helical=
```

```
    true, kx=0.5, ky=0.5};
RAD1_U4:  UNDULATOR = {lambdau=0.055, nwig=44, aw = input_awrad4, helical=true, kx=0.5, ky=0.5};
RAD1_U5:  UNDULATOR = {lambdau=0.055, nwig=44, aw = input_awrad5, helical=true, kx=0.5, ky=0.5};
RAD1_U6:  UNDULATOR = {lambdau=0.055, nwig=44, aw = input_awrad6, helical=true, kx=0.5, ky=0.5};

# DRIFTS
RAD1_D1:  DRIFT = {l = 0.440};
RAD1_D2:  DRIFT = {l = 0.550};

# QUADRUPOLES
RAD1_Q1:  QUADRUPOLE = { l = 0.22, k1= -0.68};
RAD1_Q2:  QUADRUPOLE = { l = 0.22, k1=  0.70};

# Radiators
RAD1_1:   LINE = {RAD1_U1, RAD1_D1, RAD1_Q1, RAD1_D2};
RAD1_2:   LINE = {RAD1_U2, RAD1_D1, RAD1_Q2, RAD1_D2};
RAD1_3:   LINE = {RAD1_U3, RAD1_D1, RAD1_Q1, RAD1_D2};
RAD1_4:   LINE = {RAD1_U4, RAD1_D1, RAD1_Q2, RAD1_D2};
RAD1_5:   LINE = {RAD1_U5, RAD1_D1, RAD1_Q1, RAD1_D2};
RAD1_6:   LINE = {RAD1_U6};

#------------------------------------------------------------
#FEL1_RAD:  LINE = {RAD1_1,RAD1_2,RAD1_3,RAD1_4,RAD1_5,RAD1_6,FIELDDUMP};
FEL1_RAD:  LINE = {RAD1_1,RAD1_2,RAD1_3,RAD1_4,RAD1_5,RAD1_6};
3radFEL1:  LINE = {RAD1_1,RAD1_2,RAD1_3};
RADIATOR: LINE = {RAD1_1,BEAMDUMP,RAD1_2,BEAMDUMP,RAD1_3,BEAMDUMP,RAD1_4,BEAMDUMP,RAD1_5,BEAMDUMP,RAD1_6,BEAMDUMP};

MOD_RAD1: LINE = {FEL1_MOD,RAD1_1,ALLDUMP};
RADS:  LINE = {RAD1_2,RAD1_3,RAD1_4,RAD1_5,RAD1_6};

FEL1_RAD1:  LINE = {RAD1_1,ALLDUMP};
FEL1_RAD2:  LINE = {RAD1_2,ALLDUMP};
FEL1_RAD3:  LINE = {RAD1_3,ALLDUMP};
FEL1_RAD4:  LINE = {RAD1_4,ALLDUMP};
FEL1_RAD5:  LINE = {RAD1_5,ALLDUMP};
FEL1_RAD6:  LINE = {RAD1_6,ALLDUMP};

#============================================================
# COMPLETE BEAMLINE
#============================================================
FullFEL1:   LINE = {FEL1_MOD,FEL1_RAD};
#============================================================
```

C Additional Figures

Baseline Analysis Plots

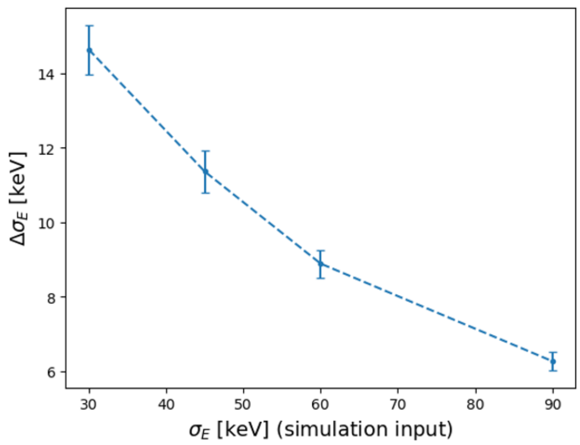

(a)

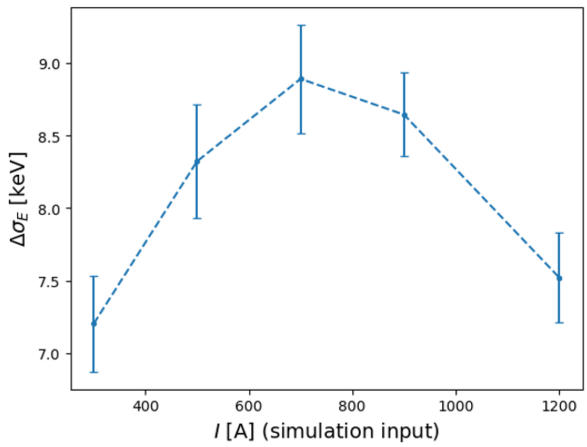

(b)

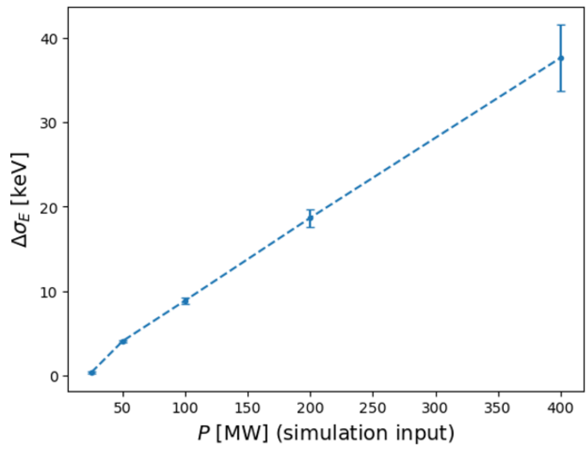

(c)

Figure 16: The deviation $\Delta\sigma_E = \sigma_{E,\text{fit}} - \sigma_{E,\text{sim}}$ as a function of (a) σ_E (while $I = 700$ A, $P = 100$ MW), (b) I (while $\sigma_E = 60$ keV, $P = 100$ MW), and (c) P (while $\sigma_E = 60$ keV, $I = 700\,$A). The error bars represent the 1σ uncertainties obtained from the covariance matrix of the fit.

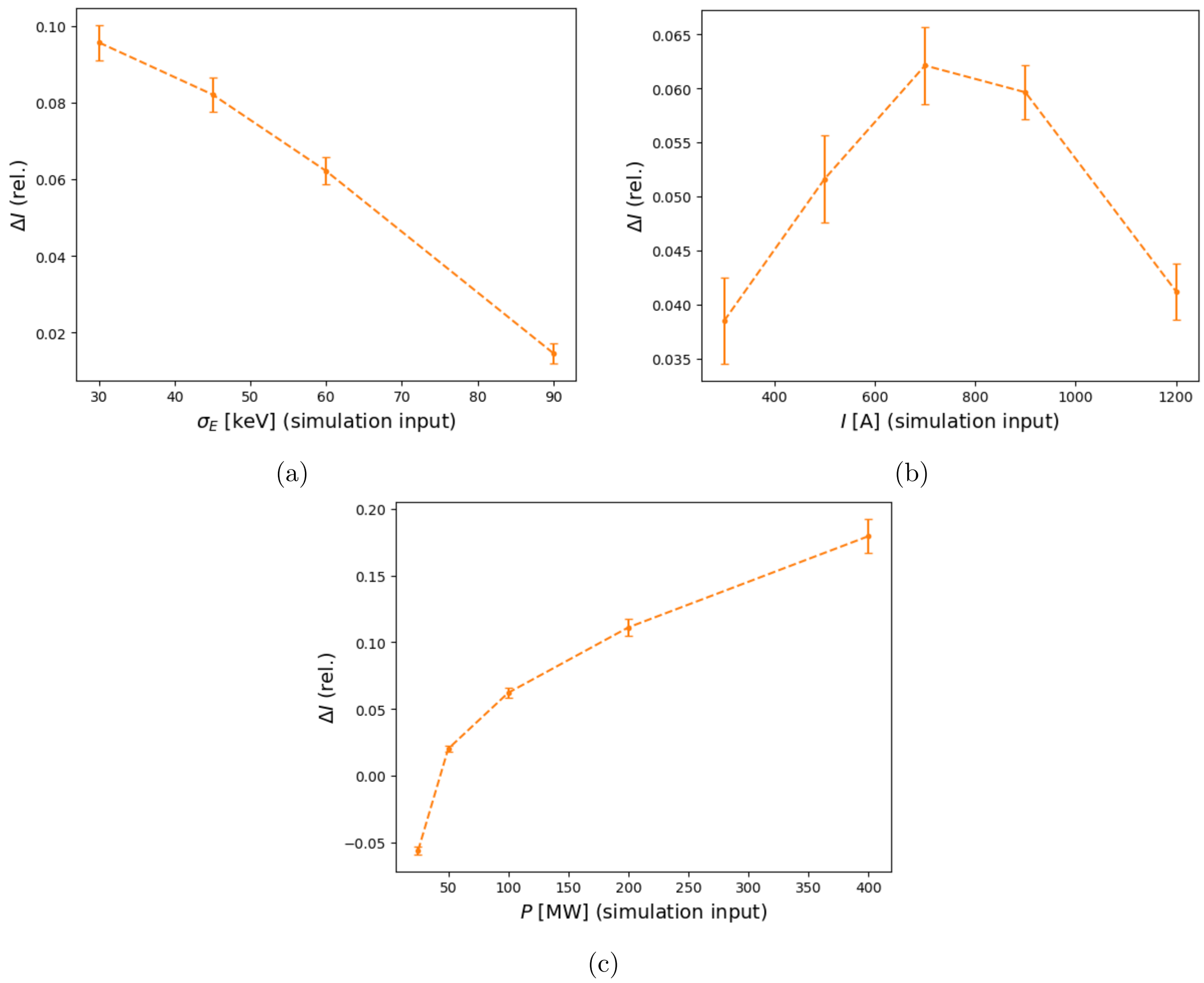

Figure 17: The deviation $\Delta I = I_{\text{fit}} - I_{\text{sim}}$ as a function of (a) σ_E (while $I = 700$ A, $P = 100$ MW), (b) I (while $\sigma_E = 60$ keV, $P = 100$ MW), and (c) P (while $\sigma_E = 60$ keV, $I = 700$ A). The error bars represent the 1σ uncertainties obtained from the covariance matrix of the fit.

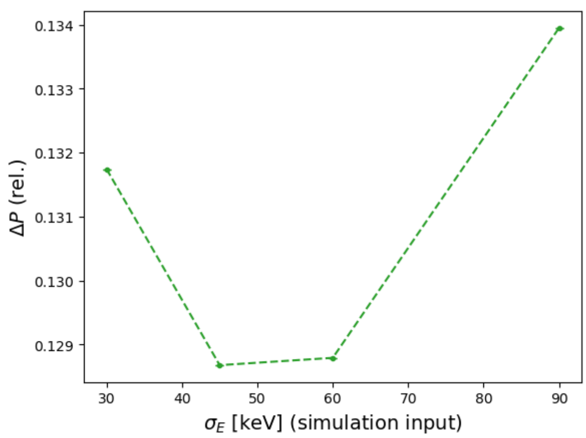

(a)

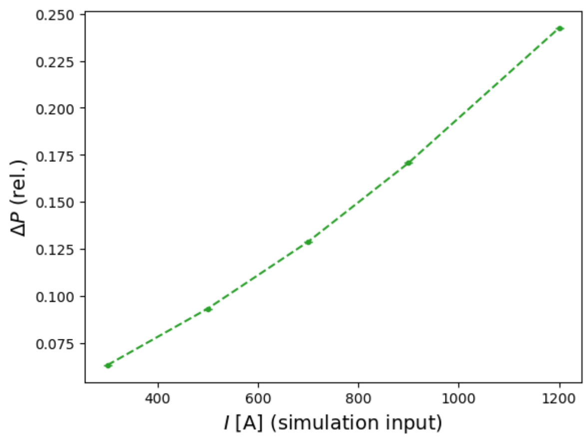

(b)

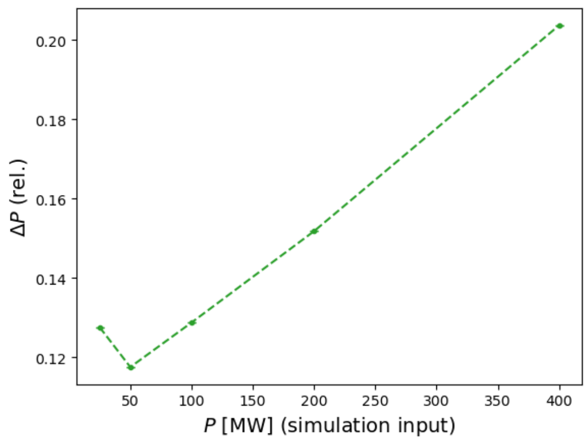

(c)

Figure 18: The deviation $\Delta P = P_{\text{fit}} - P_{\text{sim}}$ as a function of (a) σ_E (while $I = 700$ A, $P = 100$ MW), (b) I (while $\sigma_E = 60$ keV, $P = 100$ MW), and (c) P (while $\sigma_E = 60$ keV, $I = 700$ A). The error bars represent the 1σ uncertainties obtained from the covariance matrix of the fit.